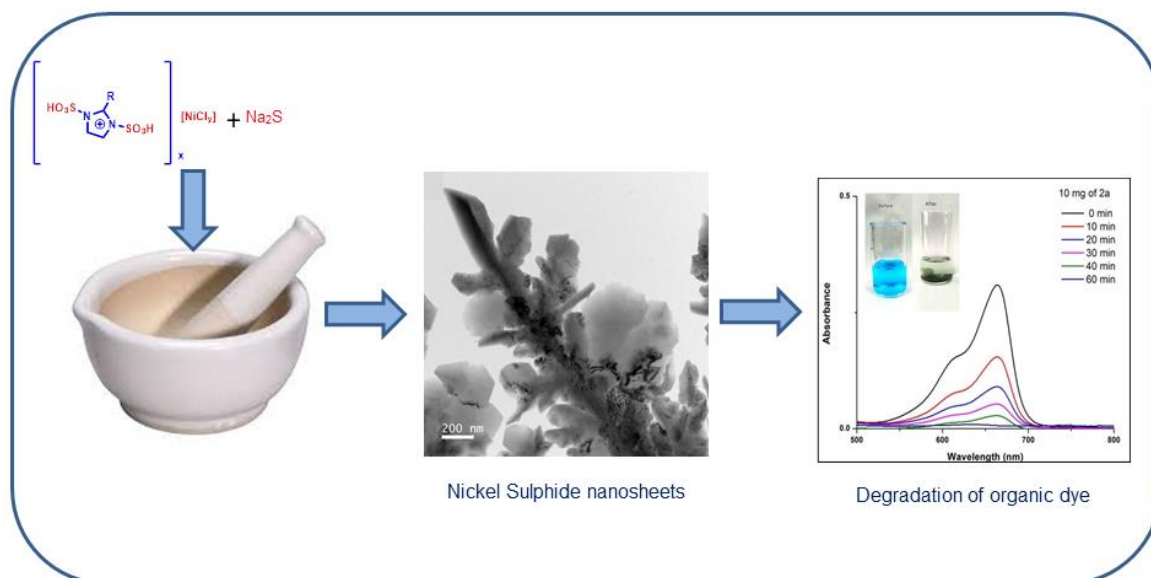


Chapter 6

Investigation of Photocatalytic Activities of Nickel Sulphide Nanosheets Synthesized using Imidazolium Based Chloronickellate Ionic Liquids as Precursor/Template for Photocatalytic Degradation of Organic Dyes



6.1 Introduction

Nanoparticles or nanomaterials have gathered immense attention from the researchers and industries alike owing to their multiple fascinating properties like large surface area, lower melting points, specific magnetization, high mechanical strength and specific optical properties [1]. The chemical and physical properties of the nanoparticles are remarkably different compared to their bulk materials. The metallic nanoparticles have found numerous industrial and biological applications like catalysis, fuel cells, batteries, drug delivery, sensors, and biosensors [2-6]. With growing significance of the metal nanoparticles in almost all branches of science and technology, the need for development of greener methods for their synthesis has also increased. In this regard, the use of ionic liquids (ILs) in nanoparticle synthesis has received considerable attention from the researchers. The inherent amphiphilicity of ILs due to the existence of distinct hydrophilic and hydrophobic molecular fragments makes them display characteristics similar to classical surfactants. This surfactant-like property of the ILs along with their ability to form H-bonding interactions, presence of large number of charge carriers and tunable polarity have been utilized successfully in their applications as solvents/capping agents for the preparation of a variety of nanoparticles including quantum dots (QDs) [7-10]. Furthermore, based on the nature and degree of these interactions between ionic liquids and nanoparticles, the size distribution and morphology of metal nanoparticles gets significantly affected. The nature of the constituent ions and the physiochemical properties of the ionic liquids are mainly known to control these ionic liquid-nanoparticle interactions as already mentioned in **Chapter 1, section 1.3.2** [11, 12].

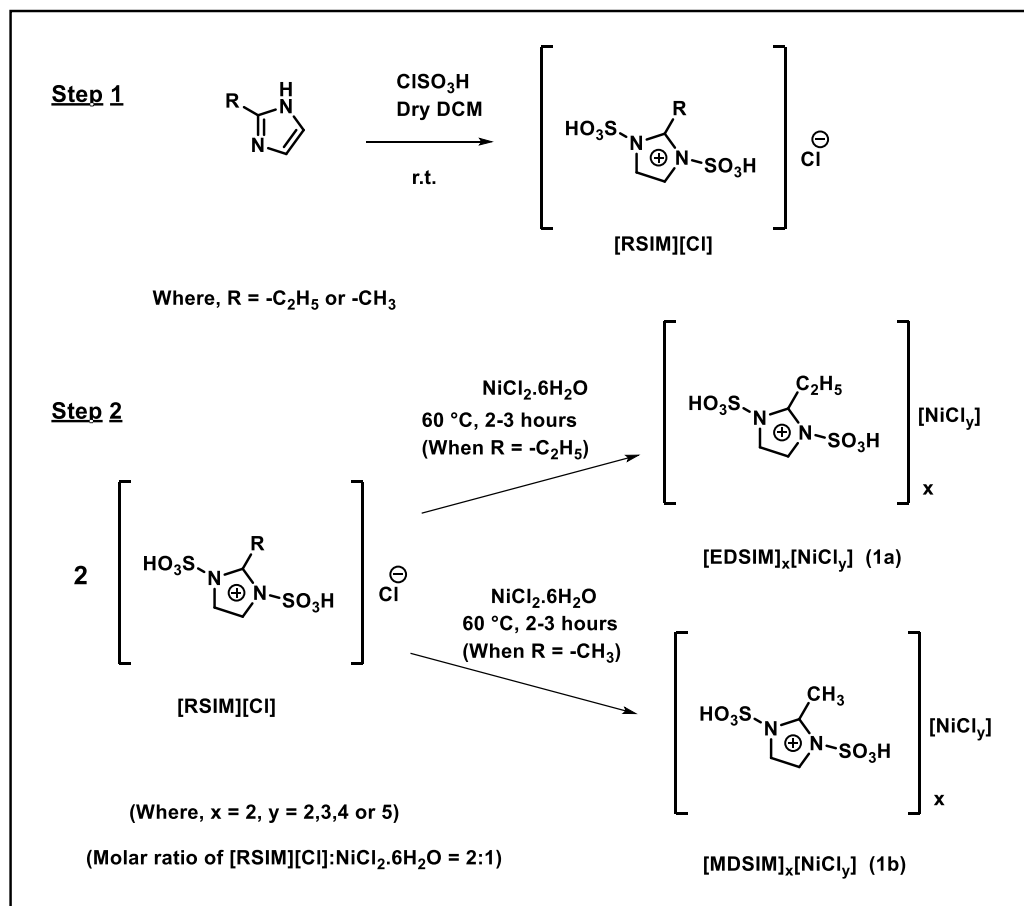
Apart from the uses of ionic liquids as solvents or capping agents in nanoparticle synthesis, especially the metal containing halometallate ILs have been utilised as precursors/templates in nanoparticle synthesis [3, 13-15]. These halometallate ionic liquids (IL) are considered as functional materials for their distinct and potentially useful properties [16, 17]. The specific characters of such ionic liquids depend on both the nature of metal present and the ratio of metal chloride to organic chloride salt used in their synthesis. The anionic component $[M_xX_y]^{n-}$ of the halometallate ILs can be varied by considering these two factors and thereby, control its stability and catalytic activity using Lewis acidity or basicity for a given composition. The characteristics and individual properties of these ILs provide wide uses in catalysis, nanoparticle synthesis,

electrochemistry, separation/extraction processes, and synthesis of inorganic semiconductors and conversion of biomass to energy products [18-20]. Addition of acidic or basic functional groups into the cation may further modify the characteristic properties of each halometallate IL. In this chapter, two new bifunctional Brønsted-Lewis acidic chloronickellatellate ionic salt systems **1a** and **1b** ($[\text{RSIM}]_x[\text{NiCl}_y]$, where $\text{R} = \text{C}_2\text{H}_5$ & CH_3 , $x = 2$, $y = 2,3,4$ or 5) were developed by incorporating two $-\text{SO}_3\text{H}$ groups into the imidazolium cation (**Scheme 6.1**) [21]. These chloronickellate ILs were then utilized as precursors/templates for the synthesis of nickel sulphide nanoparticles using a simple grinding method (**Scheme 6.2**) [3]. Although, there are previous reports available on the synthesis of nickel/nickel sulphide/nickel oxide nanoparticles using ionic liquids as solvents [1, 11], but no reports on the use of chloronickellate ILs as precursors/templates for the synthesis of nickel sulphide nanoparticles are available till date. The synthesized nickel sulphide nanoparticles were then evaluated for their photocatalytic activity in degradation of organic dyes, which are considered as one of the major class of water pollutants.

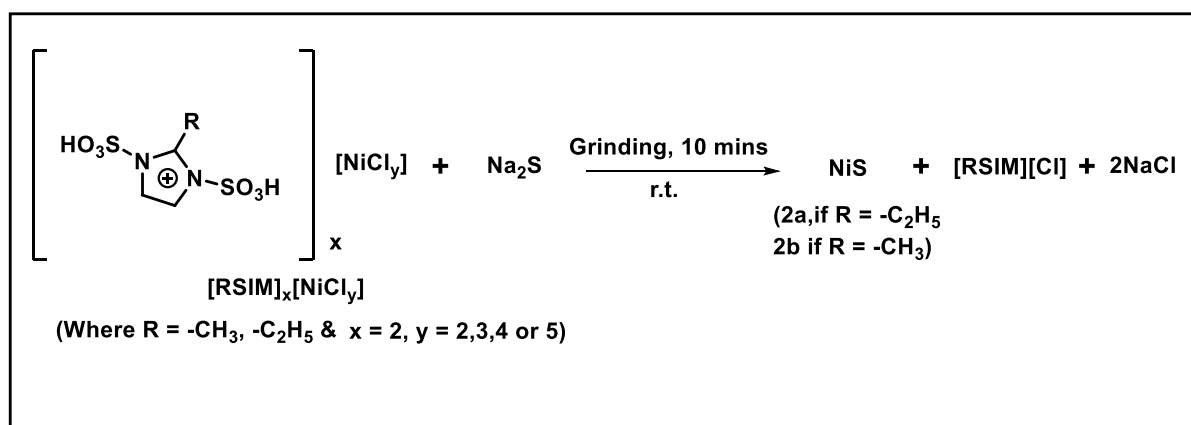
6.2 Results and Discussions

6.2.1 Characterization of N-SO₃H functionalized imidazolium based chloronickellates

Initially, the two N-SO₃H functionalized imidazolium based chloronickellates ($[\text{RSIM}]_x[\text{NiCl}_y]$, where $\text{R} = \text{C}_2\text{H}_5$ & CH_3 , $x = 2$, $y = 2,3,4$ or 5) were prepared by treatment of $\text{NiCl}_2 \cdot 6\text{H}_2\text{O}$ with the 2-methyl/2-ethyl imidazolium chloride ionic liquids obtained from step 1 in the molar ratio of 1 : 2 at 60 °C for 2-3 hours in step 2 (**Scheme 6.1**) according to the standard procedure [21]. The structural compositions of the chloronickellates were determined using NMR (¹H & ¹³C), FT-IR and ESI-Mass spectrometry.



Scheme 6.1: Synthesis of the chloronickelate ionic liquids [RSIM]_x[NiCl_y].



Scheme 6.2: Synthesis of nickel sulphide nanoparticles from [RSIM]_x[NiCl_y].

6.2.1.1 FT-IR analysis

The FT-IR spectra of both **1a** and **1b** (Fig. 6.1) detected three strong absorption bands between 1195-1170, 1040-1063 and 570-580 cm⁻¹ corresponding to S-O asymmetric stretching, symmetric stretching and bending vibrations of the -SO₃H groups associated

with the 2-alkylimidazolium cation [21]. The C-H stretching vibrations of the alkyl substituents and imidazolium cations were observed in the range of 2919–2929 cm^{-1} . The N-S and C-C stretching vibrations of the imidazolium cations were assigned at 870–880 cm^{-1} and 1620–1640 cm^{-1} respectively. The broad O-H peak around 3400 cm^{-1} represented extensive intermolecular H-bonding among the IL molecules.

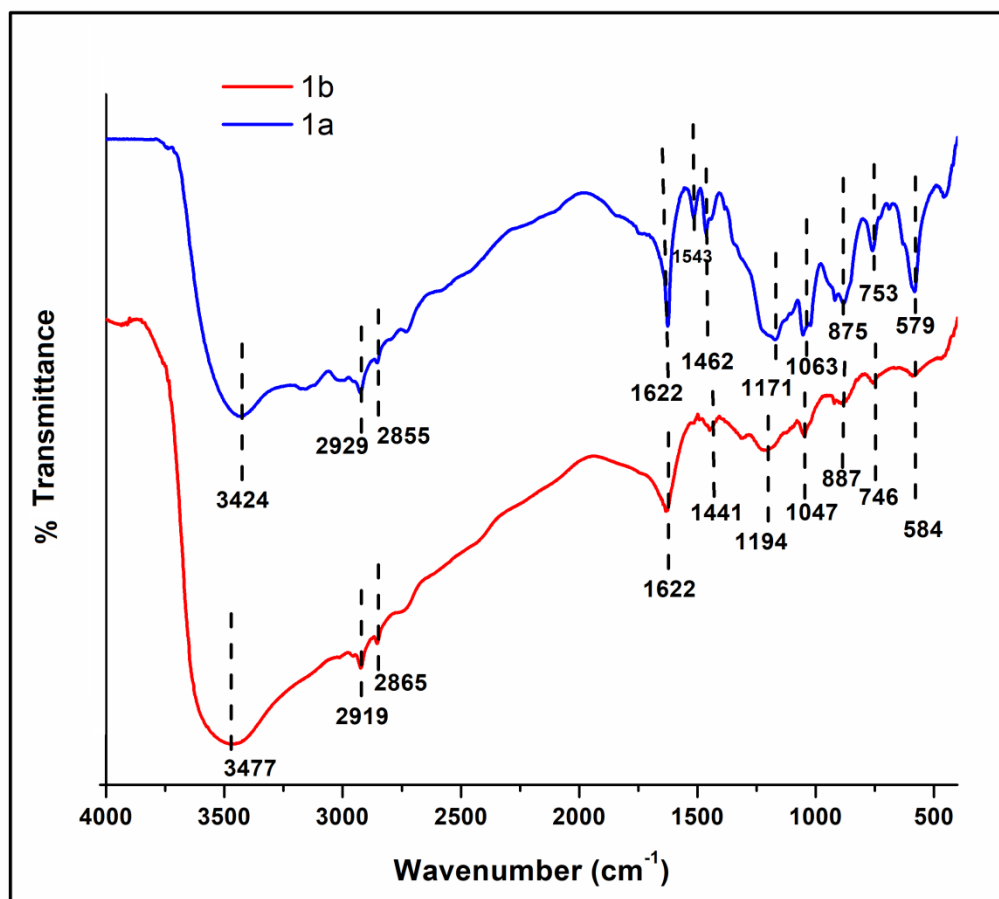
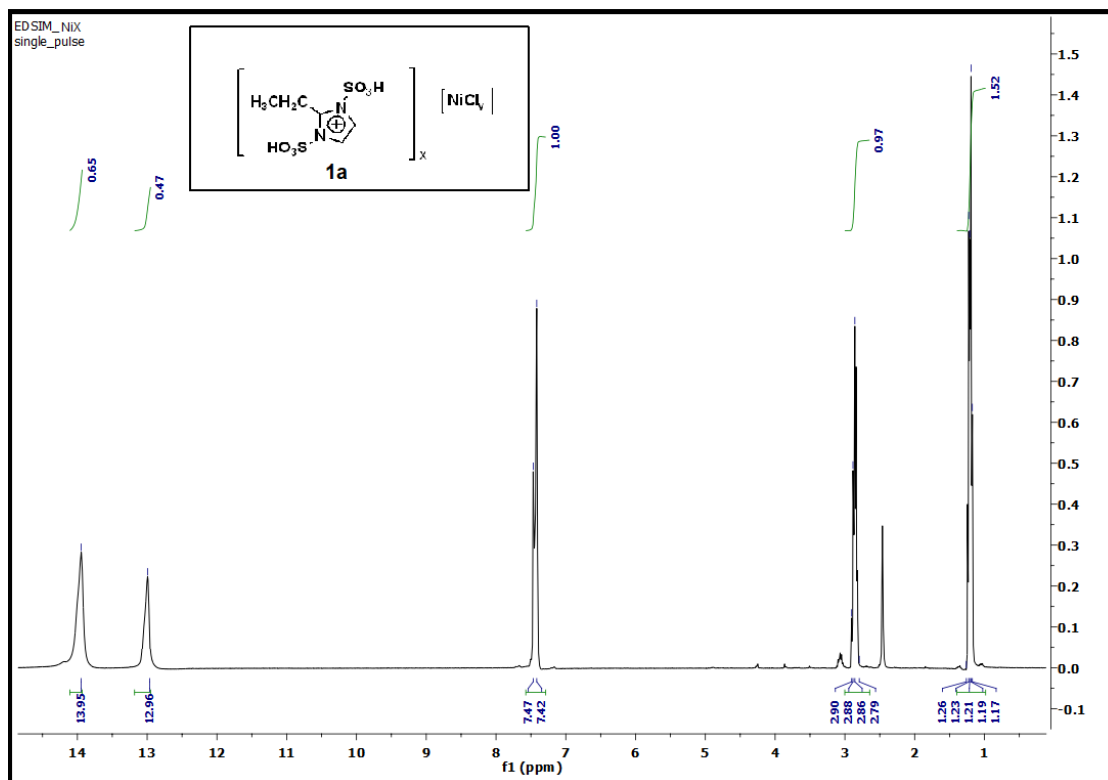
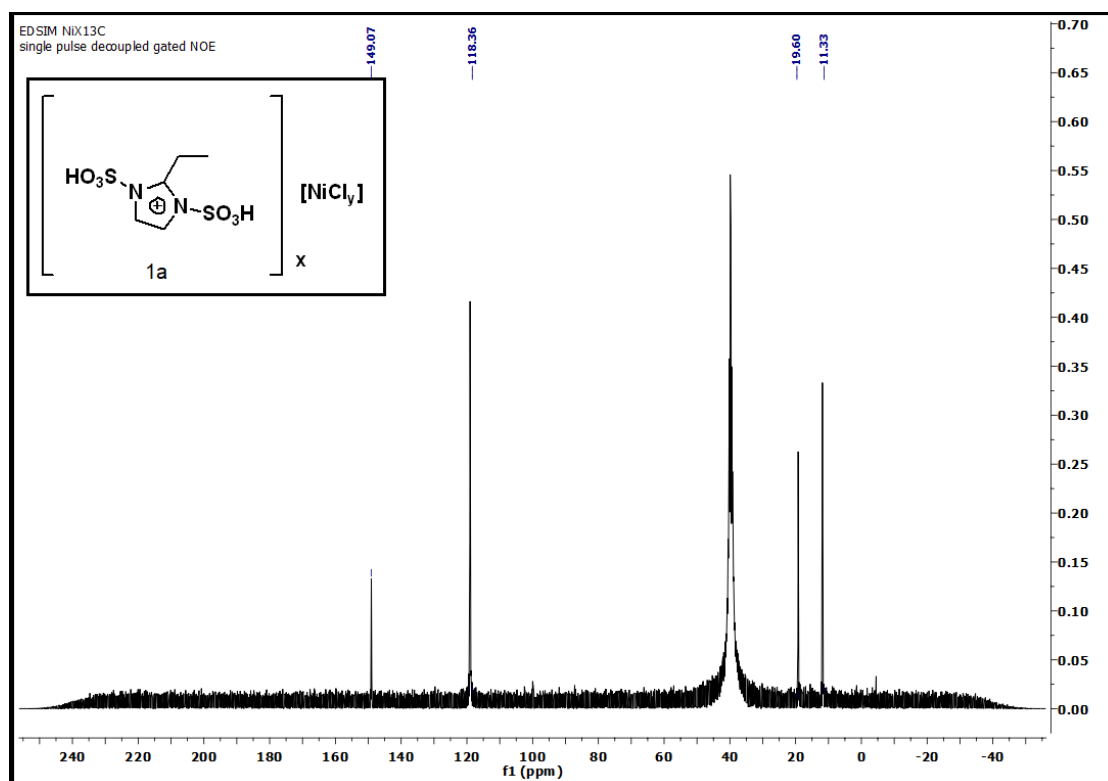


Fig. 6.1: FT-IR spectra of 1a and 1b.

6.2.1.2 NMR analysis

Two single proton peaks in the ^1H NMR spectra of the chloronickellates **1a** and **1b** around 14.3–11.9 ppm confirmed the attachment of two $-\text{SO}_3\text{H}$ groups through nitrogen atom of the imidazolium cation. Other characteristic signals of the imidazolium protons and C-2 alkyl groups were observed in the aromatic and aliphatic regions respectively. The characteristic signals of the alkyl substituents and imidazolium ring carbons were observed in the ^{13}C NMR spectra of **1a** and **1b**. **Fig. 6.2** displays the ^1H and ^{13}C NMR spectra of **1a**.

Fig. 6.2 (A): ^1H NMR spectra of **1a**.Fig. 6.2 (B): ^{13}C NMR spectra of **1a**.

6.2.1.3 ESI-Mass spectrometry analysis

The compositions of halometallates (**1a** & **1b**) were determined using ESI-mass spectrometry. The ESI-mass spectra of **1a** shows a peak at m/z 721.2721 corresponding to $[\text{EDSIM}]_2[\text{NiCl}_4]$. This indicates the presence of tetrahedral Ni(II) chloride anion $[\text{NiCl}_4]^{2-}$. Its fragmentation peaks could be observed near m/z 719.3081. In addition to this, the peak at m/z 701.4686 corresponding to $[\text{EDSIM}]_2[\text{NiCl}_3(\text{H}_2\text{O})]$ was observed. Similarly the peaks at m/z 735.2849 and 751.2576 could be assigned to $[\text{EDSIM}]_2[\text{NiCl}_4(\text{H}_2\text{O})]$ and $[\text{EDSIM}]_2[\text{NiCl}_5]$ respectively, indicating the presence of nickel in Ni(III) oxidation state.

In case of the **1b**, the peak around m/z 679.4618 could be assigned to $[\text{MDSIM}]_2[\text{NiCl}_3(\text{H}_2\text{O})]$. Additional peaks observed around m/z 717.4169 and 905.6121 could be assigned to complex species like $[\text{MDSIM}]_2[\text{NiCl}_4(\text{H}_2\text{O})]$ and $[\text{MDSIM}]_3[\text{NiCl}_2(\text{H}_2\text{O})_2]$ respectively which are present in minute amounts. **Section 6.4.6** displays the ESI mass spectra of **1a** and **1b**.

6.2.2 Characterization of the nickel sulphide nanoparticles

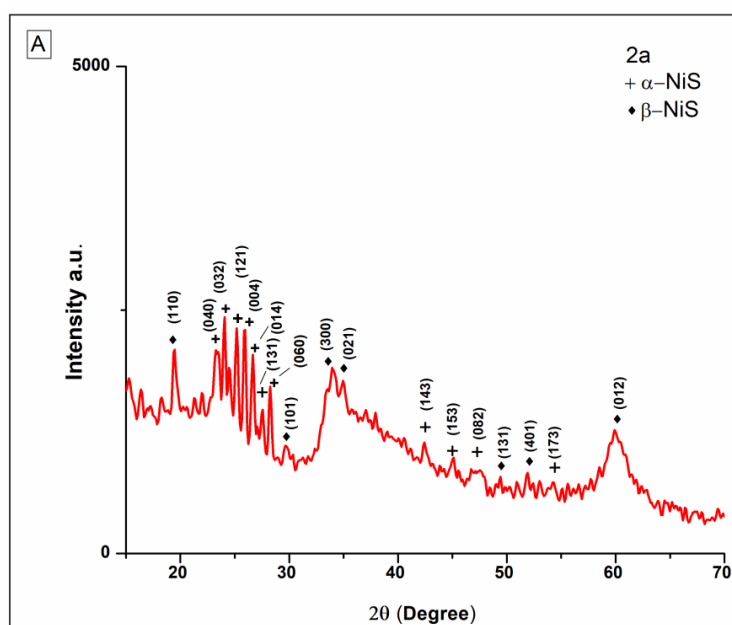
The nickel sulphide nanoparticles were synthesized according to **Scheme 6.2** by grinding of equimolar amount of $[\text{RSIM}]_x[\text{NiCl}_y]$ and sodium sulphide (Na_2S) in a mortar for 10 minutes at room temperature [3]. Here the $[\text{RSIM}]_x[\text{NiCl}_y]$ chloronickellates not only act as a metal ion precursor but also acts as a structure directing template. The size and shape of the nanoparticles can be regulated by controlling their growth and preventing their agglomeration. These $-\text{SO}_3\text{H}$ functionalized ILs exhibit properties similar to surfactants and possess polar and non-polar domains. With the increase in the alkyl chain length of the IL cation, the segregation of ILs into polar and non-polar domains increases [3] and this segregation is expected to play an important role in controlling the shape, size and properties of the nanoparticles, specially in the present case, where neat chloronickellate ILs have been used. The polar domain of the ILs consisting of the cations and the counter anions develop a protective electric double layer around the nanoparticles inhibiting their aggregation [3,7]. On the other hand, the non-polar domains consisting of the hydrophobic alkyl chain point outwards. The steric hindrance for the nanoparticle towards others present in its neighbourhood increases with the increase in the alkyl chain length, which further restricts the growth of the nanoparticles. Thus, the ILs play an important role in controlling the growth, size and shape of the

nanoparticles. Additionally, a change in the alkyl chain lengths of IL cations alters their physico-chemical properties such as dielectric constant, polarity, viscosity, conductivity, electrochemical stability and density etc. These changes could further affect the size, shape and properties of the nanoparticles [3,7]. Furthermore, these chloronickellate ILs exhibit the presence of different anionic complex ions, as can be seen in their ESI mass spectra. Since, these anionic components act as the precursors for the Ni ion, so their composition as well as structure will also have an impact on the properties of the synthesised nickel sulphide nanoparticles like shape, structure, composition, band-gap etc.

The synthesized nanoparticles were characterized using PXRD, FT-IR, RAMAN, TEM, SEM-EDX, XPS, BET and UV-Visible analysis. The photocatalytic activities of these nanoparticles were then explored in the degradation of organic dyes (Methylene blue, Methyl orange, Crystal violet and Malachite green).

6.2.2.1 Powder X-ray diffraction (PXRD) analysis

The powder X-ray diffraction patterns of **2a** and **2b** are shown in **Fig. 6.3 (A & B)**. The diffraction peaks could be indexed to the rhombohedral β -NiS phase (JCPDS card no. 86-2281) and orthorhombic α -NiS phase (JCPDS card no.71-0540) indicating the formation of both the phases. The diffraction peaks of α -NiS and β -NiS phases in **Fig. 6.3 (A & B)** are indicated by + and \blacklozenge .



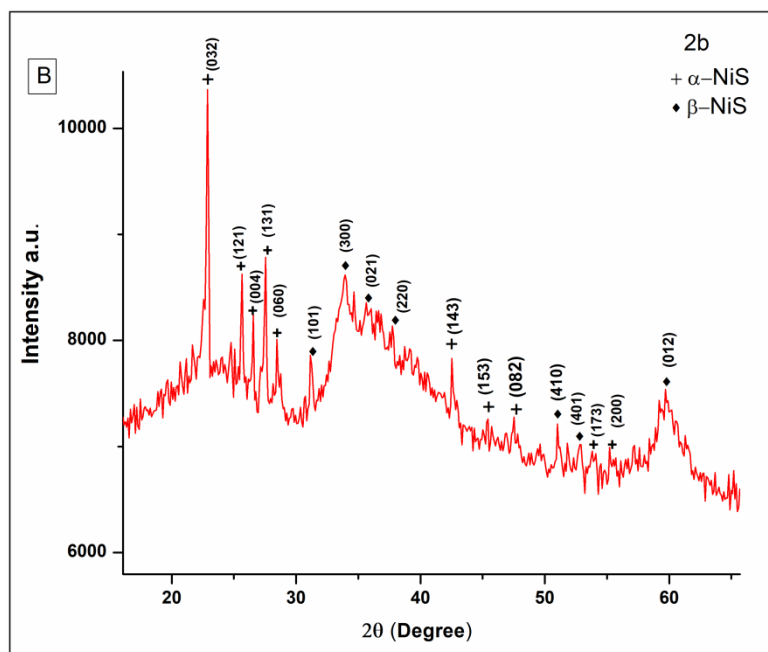


Fig. 6.3: PXR D patterns of (A) **2a** and (B) **2b**.

6.2.2.2 TEM analysis

TEM images of **2a** and **2b** (Fig. 6.4 & 6.5) reveal the formation of nickel sulphide nanosheets. The representative TEM images of **2a** shown in Fig. 6.4 (A-C) indicate the formation of leaf-like nanosheets. The selected area electron diffraction (SAED) images of **2a** and **2b** (Fig. 6.4 D & 6.5 D) show concentric ring patterns indicating their nanocrystalline nature [22]. The d-spacing ~ 0.294 nm calculated from the SAED images of **2a** and **2b** corresponds to the (101) plane of rhombohedral β -NiS [23], which is in agreement with their PXR D data Fig. 6.3 (A & B). The sizes of the nanoparticles in **2a** and **2b** ranged between 20-35 nm.

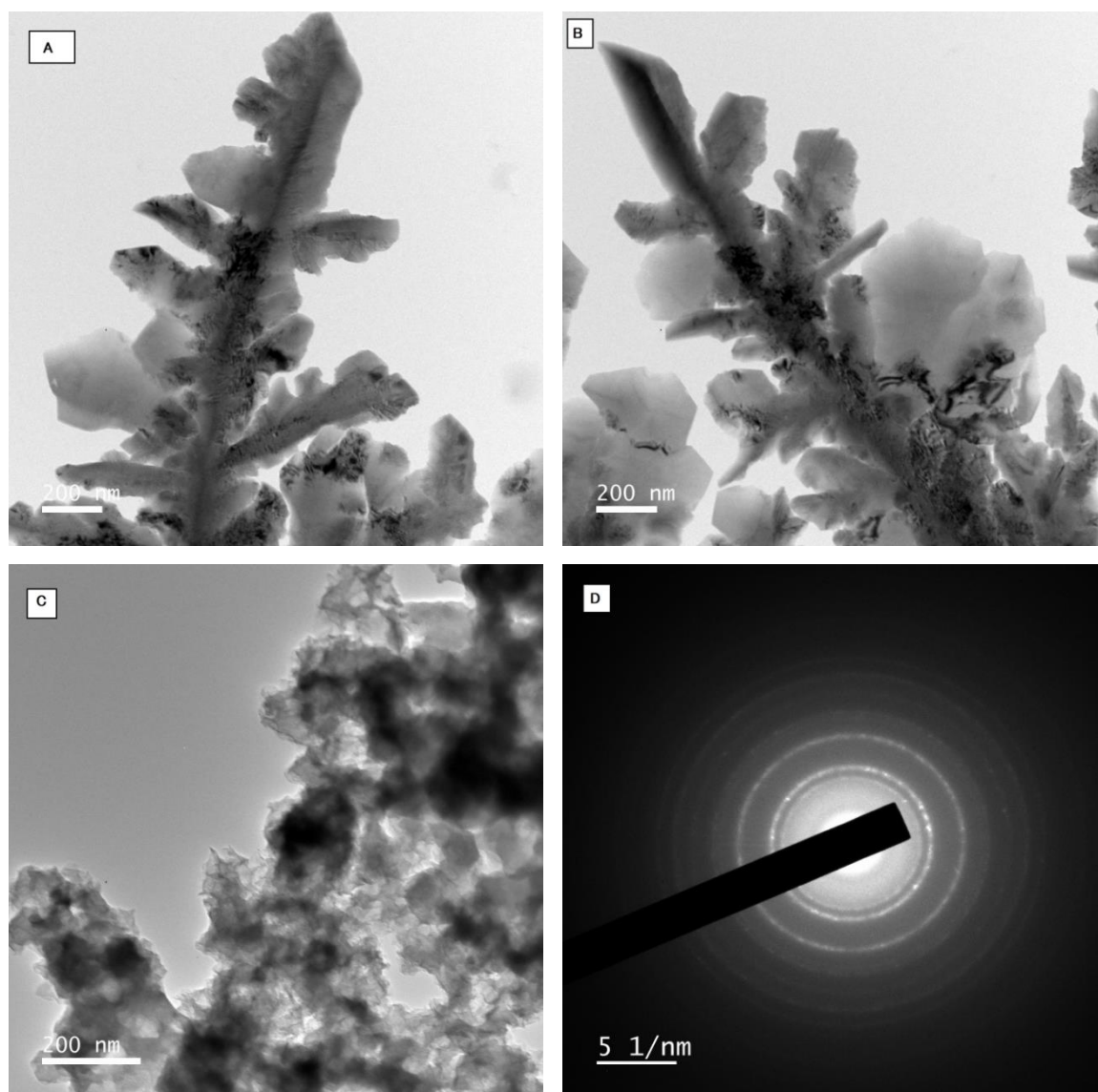


Fig. 6.4: (A), (B) & (C) TEM images of **2a**, (D) SAED image of **2a**.

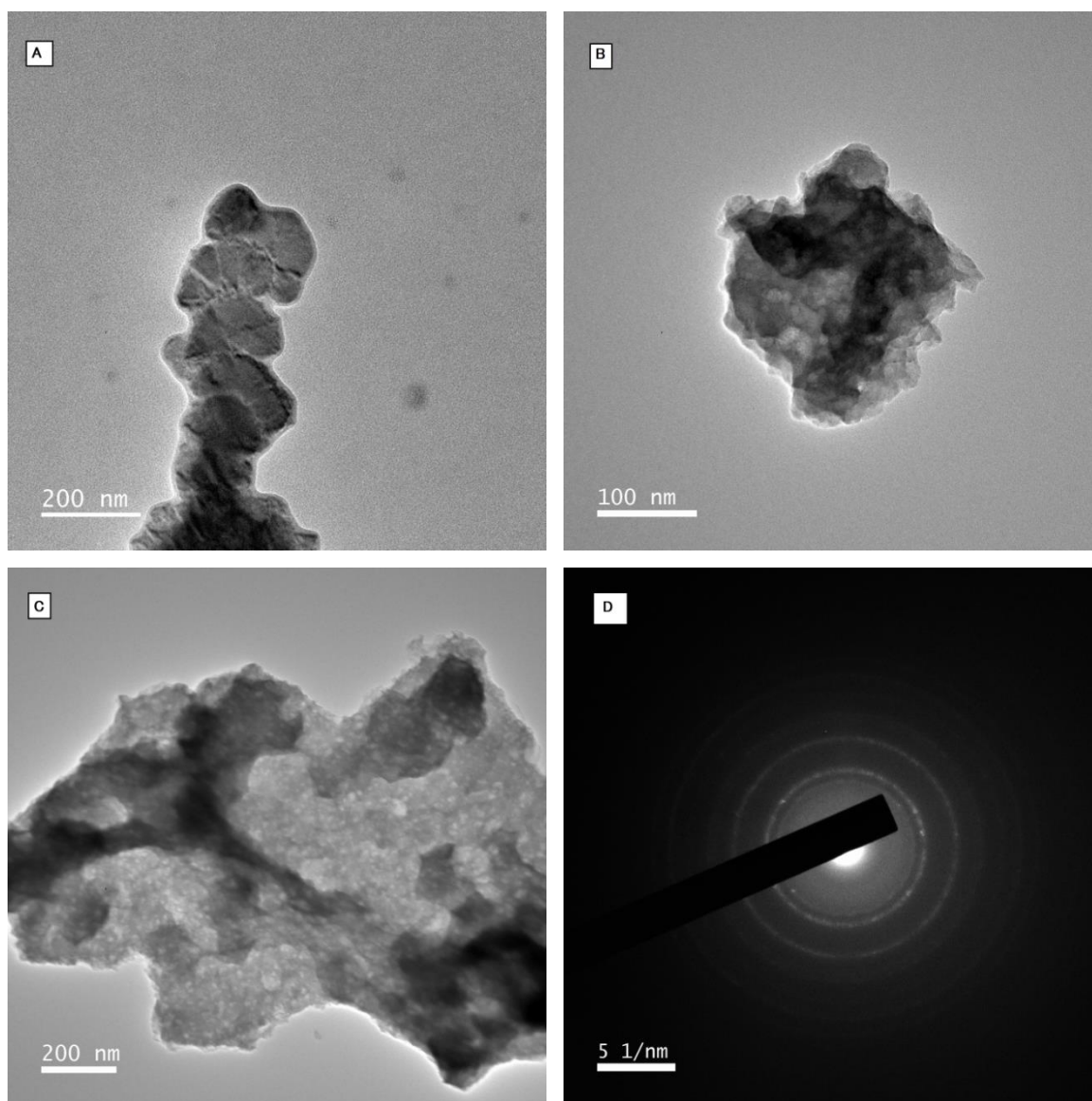


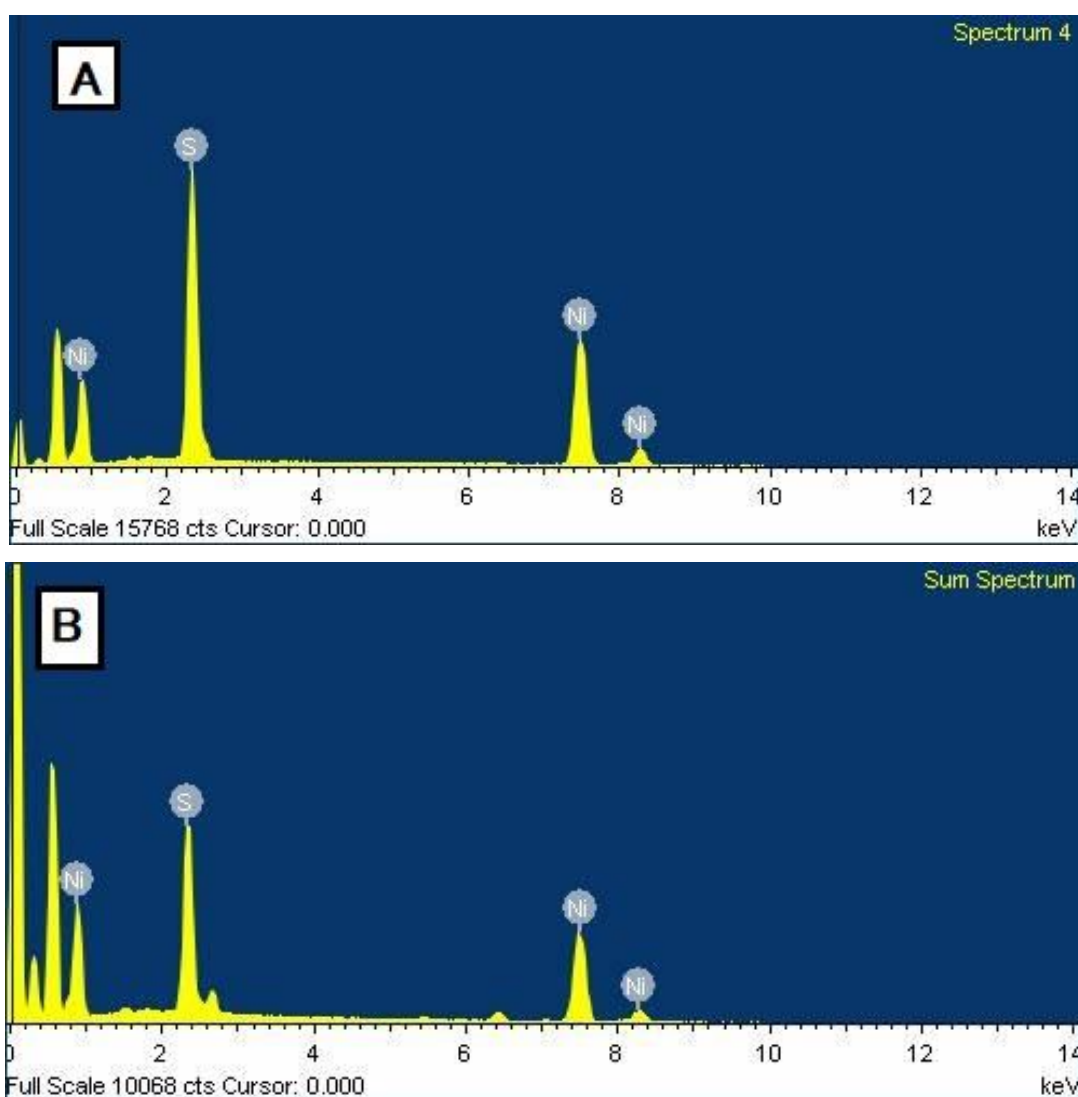
Fig. 6.5: (A), (B) & (C) TEM images of **2b**, (D) SAED image of **2b**.

6.2.2.3 EDX and SEM analysis

Energy dispersive X-ray (EDX) analysis was performed for **2a** and **2b** which confirmed the presence of nickel and sulphur in **Fig.6.6 (A & B)**. The SEM images of **2a** and **2b** (**Fig 6.7 A, B, E & F**) express a sponge-like surface morphology. The EDX elemental mapping of **2a** and **2b** (**Fig 6.7 C, D,G & H**) indicate the homogeneous distribution of Ni and S throughout the samples. The atomic percentage compositions along with the calculated weight % compositions are displayed in **Table 6.1**. The Ni:S molar ratio in **2a** is determined to be 1.08:1.00, while that of **2b** is 1.05:1.00. These values match well with the expected 1:1 nickel to sulphur molar ratio.

Table 6.1: Distribution of elements nickel and sulphur in **2a** and **2b** from EDX analysis.

Catalyst	Element weight%		Atomic %	
	Nickel	Sulphur	Nickel	Sulphur
2a	66.57	33.43	52.09	47.91
2b	65.72	34.28	51.14	48.86

**Fig. 6.6:** EDX spectra of (A) **2a** and (B) **2b**.

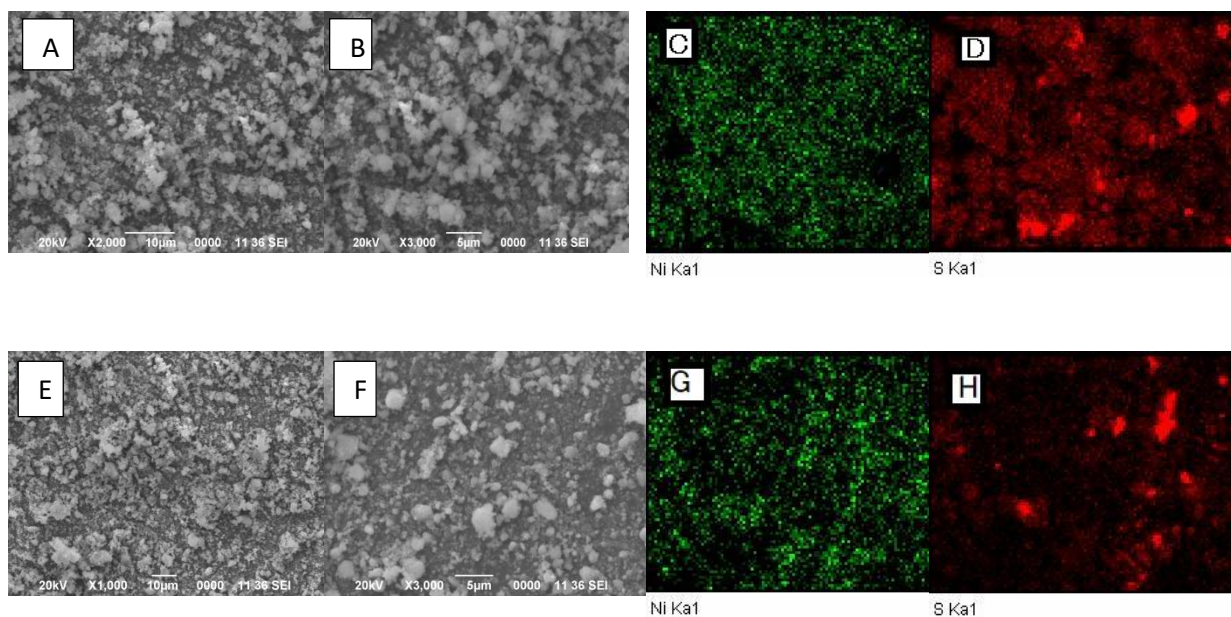


Fig. 6.7: (A) & (B) SEM images of **2a**, (C) & (D) EDX mapping of **2a**, (E) & (F) SEM images of **2b**, (G) & (H) EDX mapping of **2b**.

6.2.2.4 FT-IR analysis

Furthermore, to examine the functional groups and metal ions of the synthesized nanomaterials, the FT-IR spectra of **2a** and **2b** were recorded in $400\text{--}4000\text{ cm}^{-1}$ region (**Fig. 6.8**). FT-IR spectra of **2a** and **2b** showed peaks around 3400 cm^{-1} region and 1623 cm^{-1} corresponding to the stretching and bending vibrations of --OH group [24]. Additionally, the characteristic absorption bands observed at 1096 cm^{-1} and 608 cm^{-1} correspond to the Ni–S stretching (asymmetric and symmetric) vibration modes of sulphides [24].

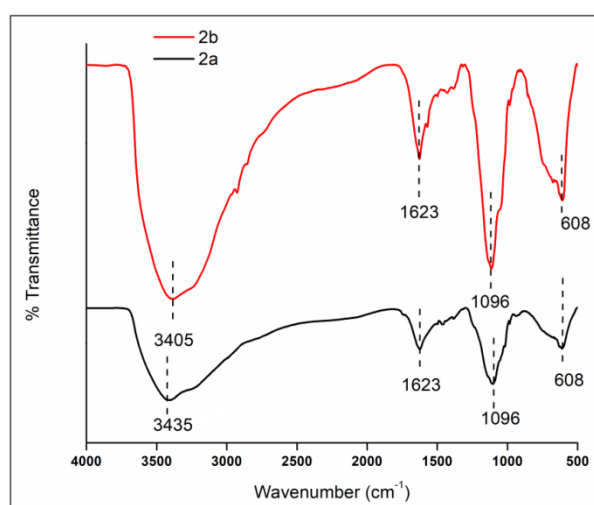


Fig. 6.8: FT-IR spectra of **2a** and **2b**.

6.2.2.5 Raman analysis

The Raman spectra of **2a** and **2b** shown in **Fig. 6.9 (A & B)** were obtained at room temperature. In case of **2a**, two vibrational modes at 148 and 240 cm^{-1} corresponding to the β -NiS phase were observed. While in case of **2b**, these vibrational modes were observed at 141 and 232 cm^{-1} . These Raman shifts are in agreement with the literature data [25]. However, some vibrational modes could not be observed. This may be due to the small size effect of the nanomaterials, since Raman vibrational modes depend on the vibration of the crystal lattice [26]. When the size of the crystal is reduced to the nanoregion, the atom arrangement inside the crystal lattice may change compared with that of the bulk materials, which would affect the vibrational modes.

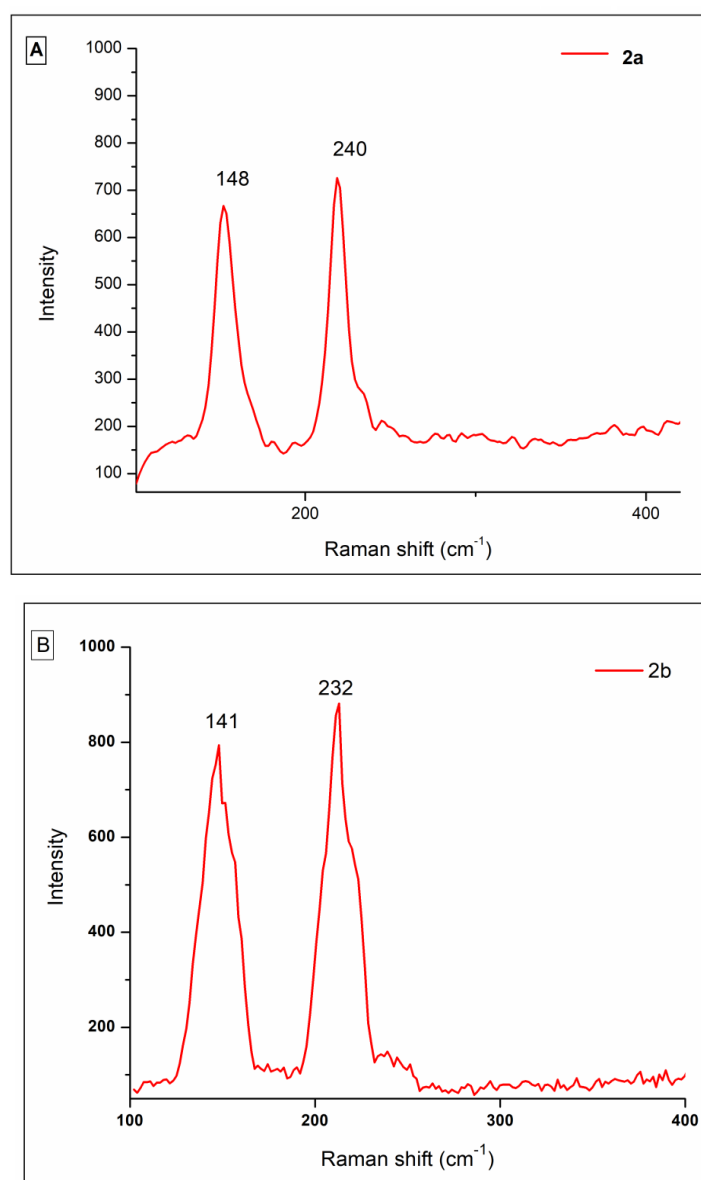


Fig. 6.9: Raman spectra of (A) **2a** and (B) **2b**.

6.2.2.6 X-ray Photoelectron spectroscopy (XPS) study

The elemental composition and chemical state of the prepared NiS nanoparticles **2a** and **2b** were studied using X-ray Photoelectron spectroscopy. The Ni 2p XP spectra of **2a** (Fig. 6.10 A) featured two prominent peaks with binding energy values 855.90 eV for Ni 2p_{3/2} and 873.49 eV for Ni 2p_{1/2} [27-29]. These signals indicated the presence of Ni²⁺ oxidation state [29]. In the S 2p XP spectra of **2a** (Fig. 6.10 B) two doublet peaks at 161.91 eV for S 2p_{3/2} and 162.80 eV for S 2p_{1/2} corresponding to S²⁻ state were observed [29, 30]. Similar peaks corresponding to S 2p_{3/2} and S 2p_{1/2} were observed at 161.71 eV and 162.78 eV in the S 2p XP spectra of **2b** (Fig. 6.10 D). Furthermore, the Ni 2p XP spectra of **2b** (Fig. 6.10 C) displayed prominent peaks at 855.73 eV for Ni 2p_{3/2} and 873.41 eV for Ni 2p_{1/2}.

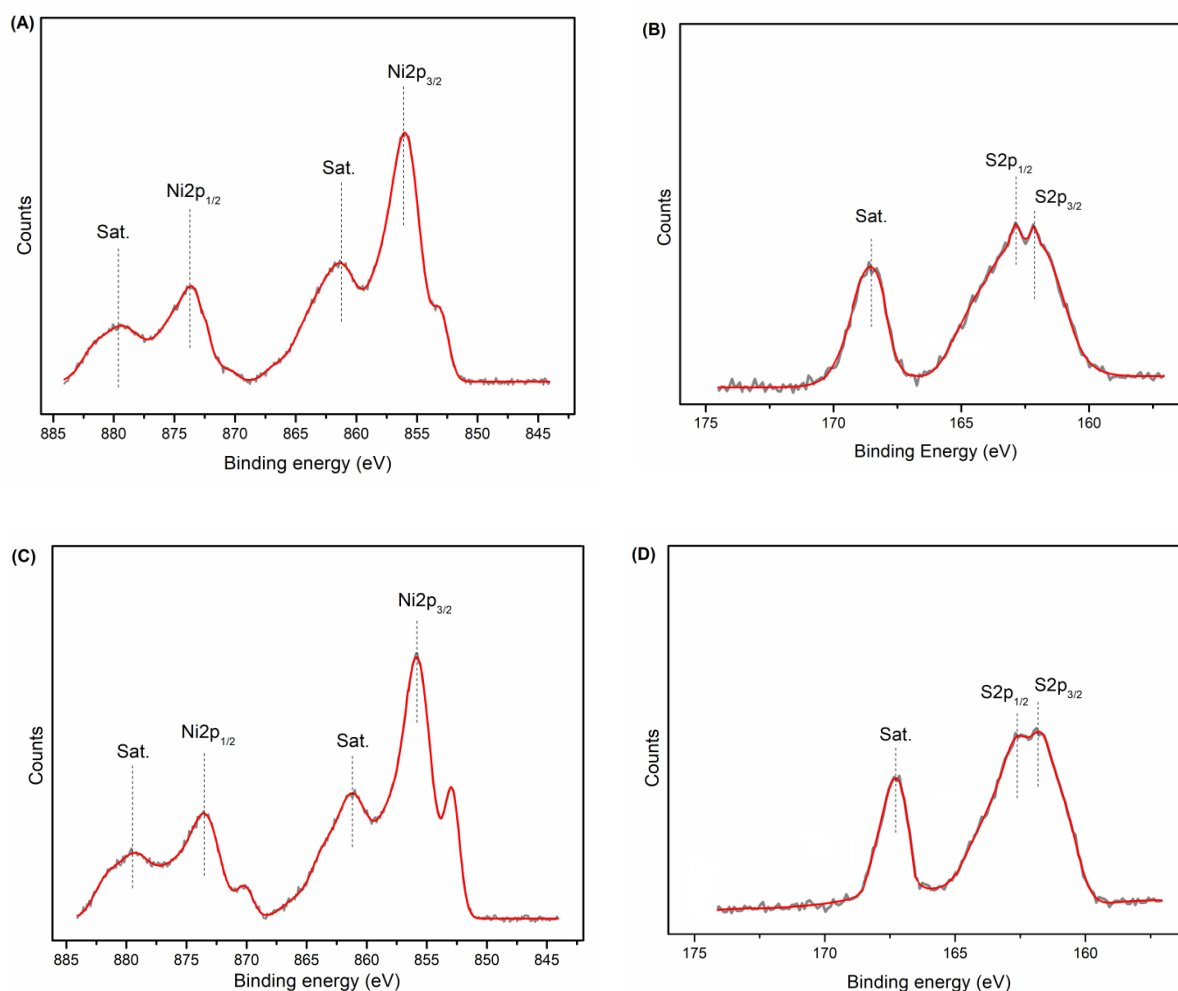


Fig. 6.10: XP spectra of (A) nickel (Ni 2p) of **2a** and (B) sulphur (S 2p) of **2a** (C) nickel (Ni 2p) of **2b** and (D) sulphur (S 2p) of **2b**.

6.2.2.7 Optical analysis

The optical band gap of the NiS nanoparticles **2a** and **2b** were analysed using the UV–visible diffuse reflectance spectra shown in **Fig.6.11 (A & B)**. From the UV data, the Tauc plots were drawn to calculate the band gap values of **2a** and **2b (Fig.6.12 (A & B))**. The Tauc plot follows the **equation 2.1 (Chapter 2)**:

$$(\alpha h\nu)^{1/n} = \beta (h\nu - E_g) \quad \text{(Equation 2.1)}$$

where α , h , ν , β and E_g are the coefficient of absorption, Planck's constant, frequency of incident photon, constant of band tailoring parameter and E_g is the energy of optical bandgap for direct ($n = 1/2$) or indirect transition ($n = 2$) [31, 32]. The power factor of transition mode 'n' is dependent on nature of solid material. The plotting of photo energy $h\nu$ versus $(\alpha h\nu)^2$ provides a straight line in certain regions by assuming all transitions as direct transitions. As per the Tauc plot, the estimated band gap value of **2a** was found to be 2.39 eV and that of **2b** was found to be 2.80 eV. The obtained results are matched well with those in the literature [27]. The NiS nanoparticles have the potential to be used as a photocatalyst.

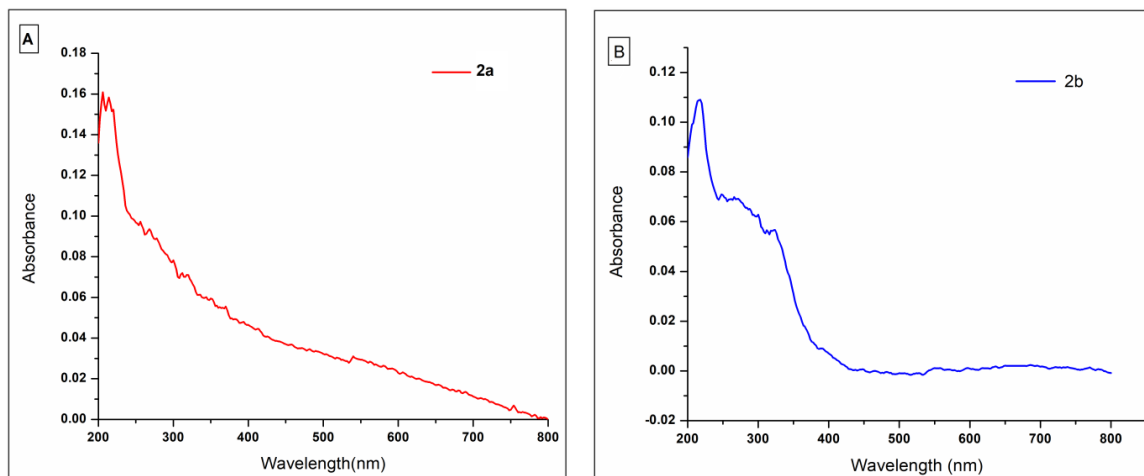


Fig. 6.11: UV–vis spectra of (A) **2a** and (B) **2b**.

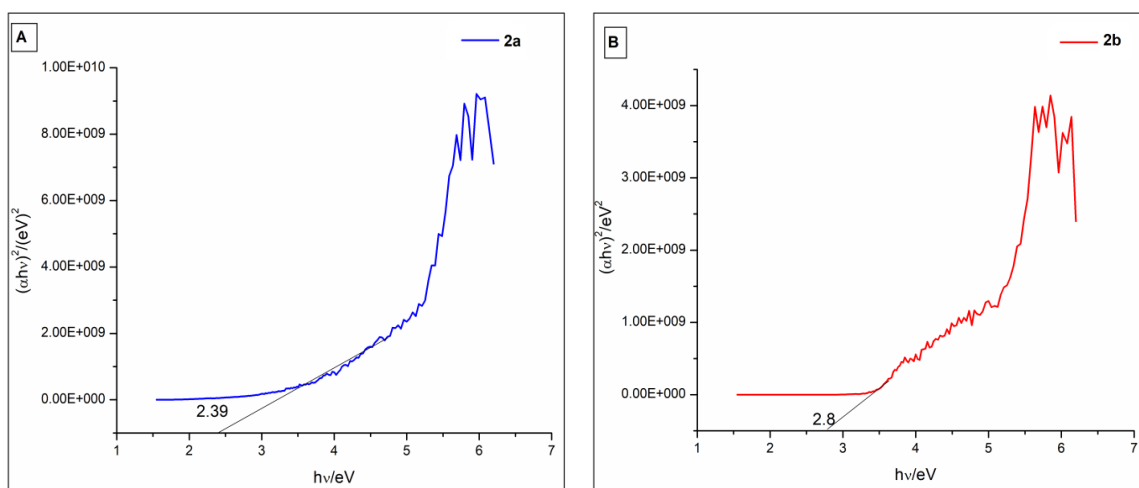


Fig. 6.12: Tauc Plot of (A) **2a** and (B) **2b**.

6.2.2.8 BET surface area analysis

Surface areas of the nickel sulphide nanosheets (**2a** and **2b**) were measured from their Brunauer Emmett Teller (BET) nitrogen adsorption-desorption isotherm (**Fig. 6.13**). The surface area values of **2a** and **2b** were found to be 22.27 m²/g and 13.68 m²/g respectively. Increase in the surface area values of the nickel sulphide nanosheets are believed to increase their catalytic activity. The pore size distribution of **2a** and **2b** were determined using the BJH (Barrett Joyner Halenda) distribution plots (**Fig. 6.13 (inset)**) from the desorption branch of the isotherms. The average pore diameter of both **2a** and **2b** were found to 3.82 nm, indicating their mesoporous nature.

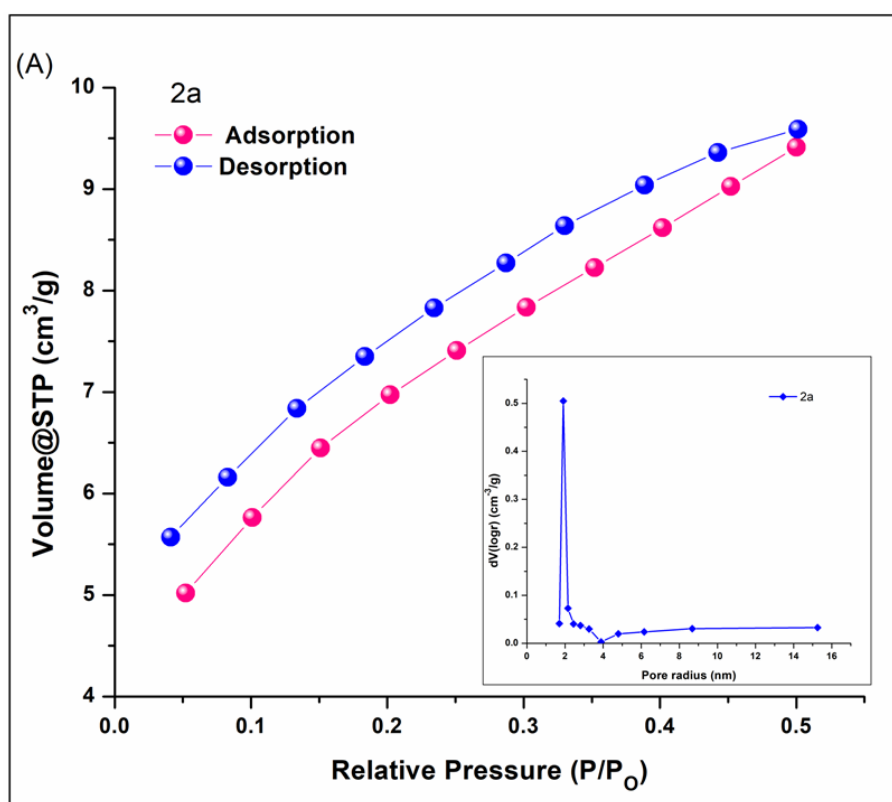
6.2.3 Catalytic study

The photocatalytic efficiency of the NiS nanoparticles **2a** and **2b** were examined in the degradation of organic dyes methylene blue (MB), methyl orange (MO), crystal violet (CV), malachite green (MG) and their mixtures. Methylene Blue was used as a model dye for optimising reaction conditions. The degradation process was monitored using UV-Vis spectroscopy. The photocatalytic catalytic activities of **2a** and **2b** for a 10 ppm MB solution were initially studied under sunlight by varying their amount (2, 5 and 10 mg). From the UV-Vis spectra of MB in **Fig. 6.14 C**, it was found that the degradation of MB was very effective in presence of 10 mg of **2a** catalyst, and 98.38% removal was achieved within 60 minutes. In case of **2b**, 93.11% removal of MB was achieved with 10 mg of **2b** within 80 minutes **Fig. 6.14 F**, thus indicating the better catalytic activity of **2a**.

These results are consistent with the lower band gap values of **2a** compared to **2b** and higher surface area values of **2a**. In absence of the catalysts, the concentration of MB remained almost constant throughout the experiments. All the reactions after this were performed using 10 mg of **2a** catalyst. The degradation rate (%) of MB was calculated using the following **Equation 6.1**:

$$\text{Degradation rate (\%)} = \{(A_0 - A_t) / A_0\} * 100 \quad (\text{Equation 6.1})$$

Where, A_0 is the absorbance at time $t = 0$ (i.e., A_0 is the absorbance of MB solution after it was kept in dark for 120 minutes in presence of the catalyst to establish the adsorption-desorption equilibrium) and A_t is the absorbance at the same wavelength at a given reaction time 't'.



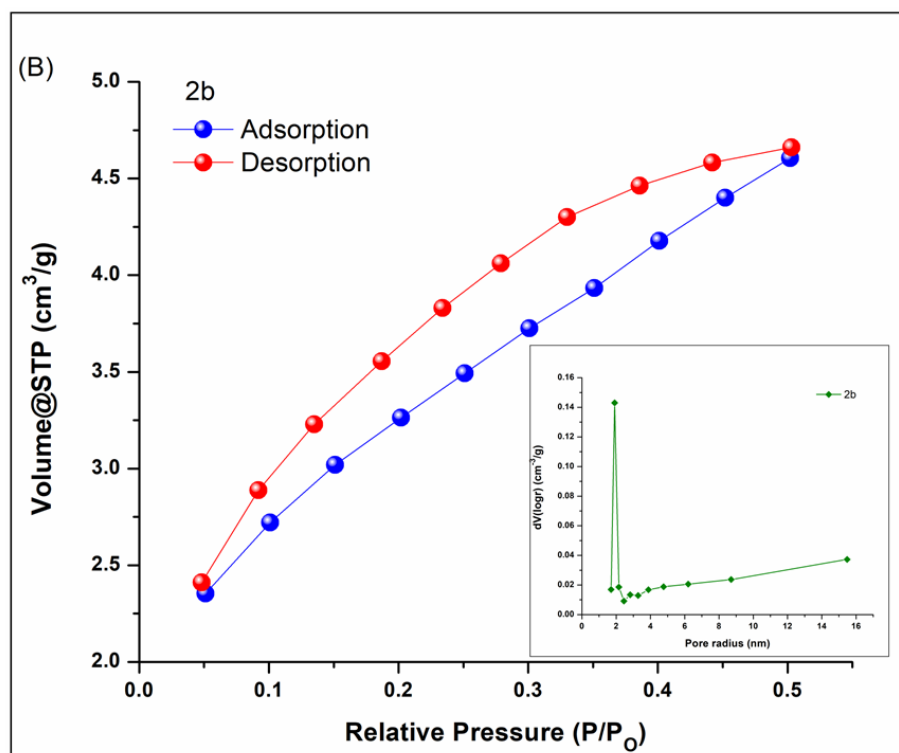


Fig. 6.13: N_2 adsorption-desorption isotherms and corresponding BJH pore size distributions (inset) of (A) **2a** and (B) **2b**.

The order of degradation of MB in presence of 10 mg of **2a** was obtained from the linear fit regression plot of $\ln(A_t/A_0)$ versus degradation time (**Fig. 6.15A**). From the correlation coefficient value $R^2 = 0.999$, it can be concluded that the photo-degradation reaction of MB dye followed pseudo first order kinetics. The rate constant k for degradation of MB by **2a** was obtained from the slope of the linear fit regression plot and was found to be $k = 0.06 \text{ min}^{-1}$. From the linear fit regression plot for degradation of MB by 10 mg of **2b** (**Fig. 6.15B**), the value of rate constant was found to be $k = 0.03 \text{ min}^{-1}$ and the correlation coefficient value was $R^2 = 0.987$, indicating pseudo first order kinetics.

Additionally, the photocatalytic efficiency of **2a** was evaluated in the degradation of other organic dyes methyl orange (MO), crystal violet (CV), malachite green (MG) and their mixtures (**Fig. 6.16**). In case of methyl orange (MO), around 70% degradation was achieved in 80 minutes in presence of 10 mg of **2a**. For crystal violet (CV) and malachite green (MG), 96.30% and 85.20% degradation were achieved respectively in 120

minutes. Furthermore, the catalyst **2a** also effectively degraded the mixtures of these dyes (MB+MO and CV+MG).

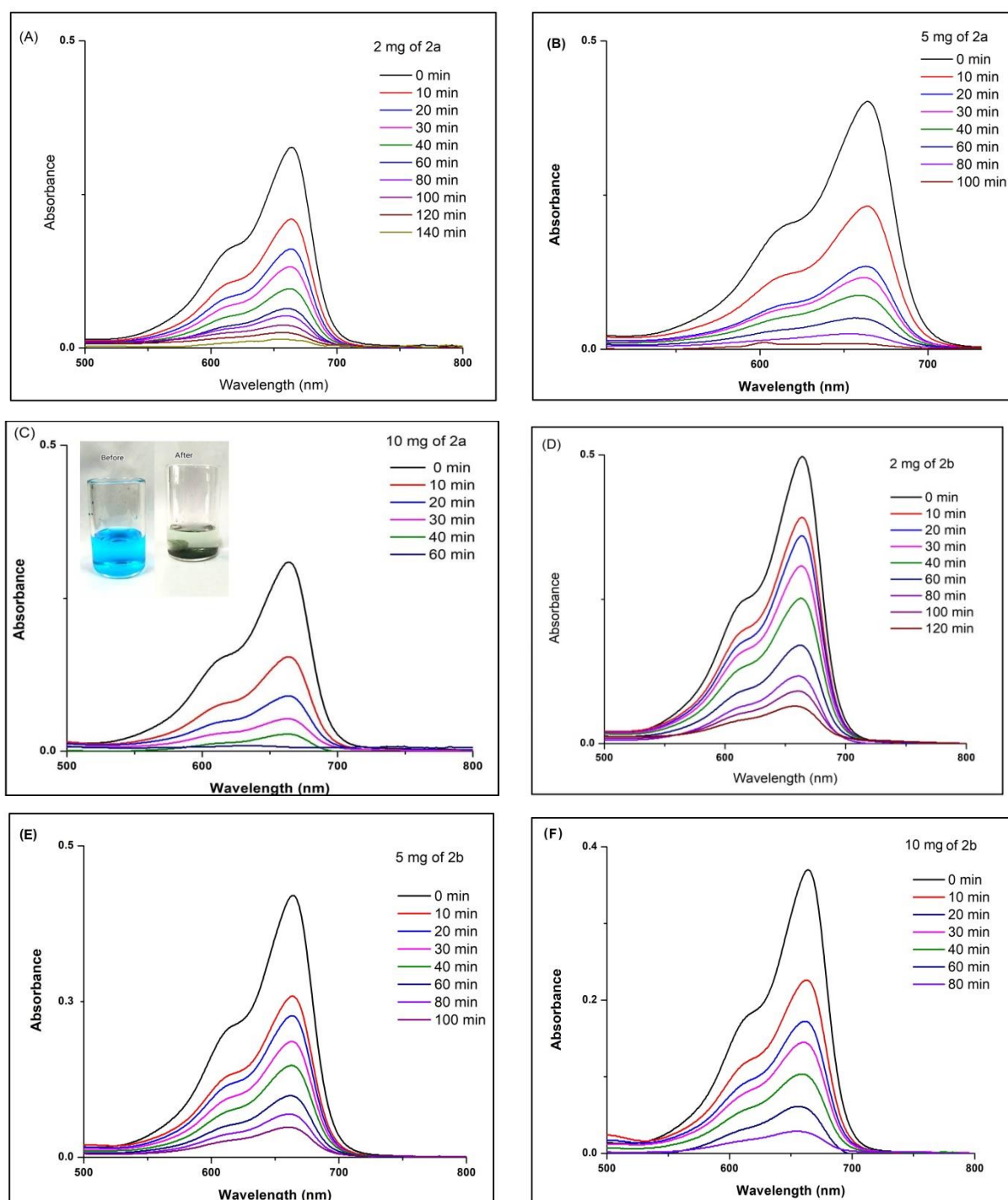


Fig. 6.14: Degradation of MB dye in presence of sunlight using (A) 2 mg of **2a**, (B) 5 mg of **2a**, (C) 10 mg of **2a**, (D) 2 mg of **2b**, (E) 5 mg of **2b**, and (F) 10 mg of **2b**, monitored by UV-Vis spectroscopy.

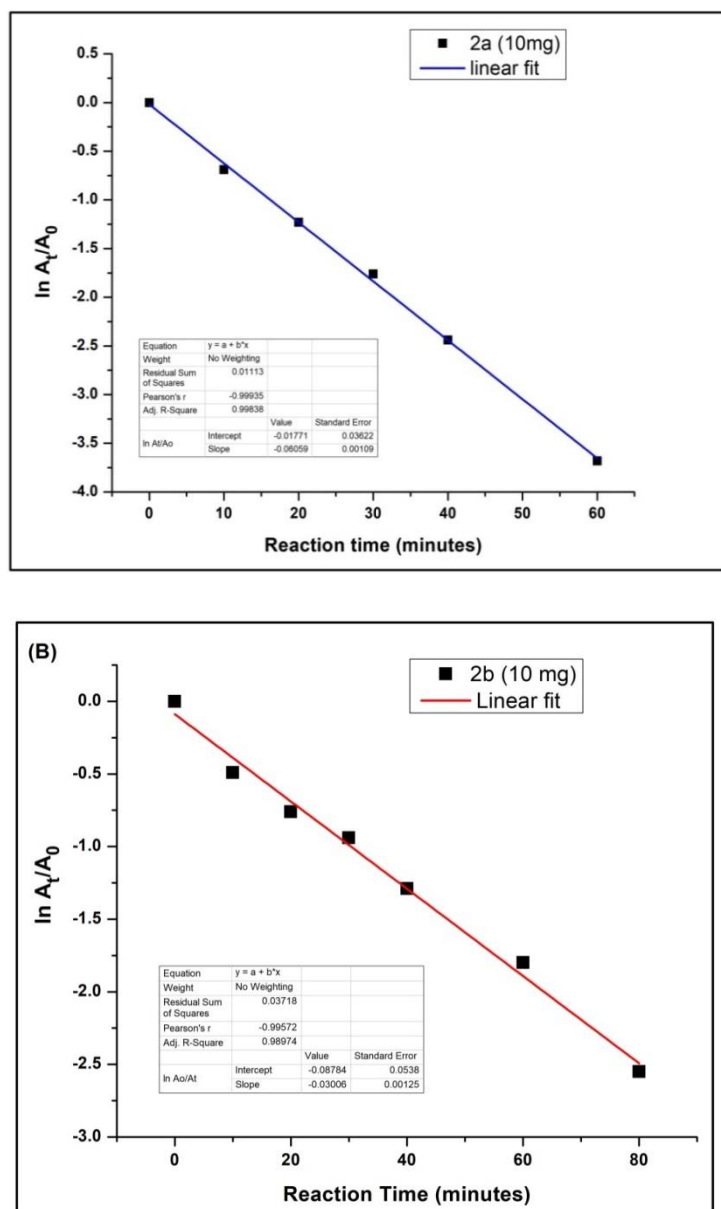


Fig. 6.15: First order linear regression plot of MB degradation under sunlight in presence of (A) 10 mg of **2a** and (B) 10 mg of **2b**.

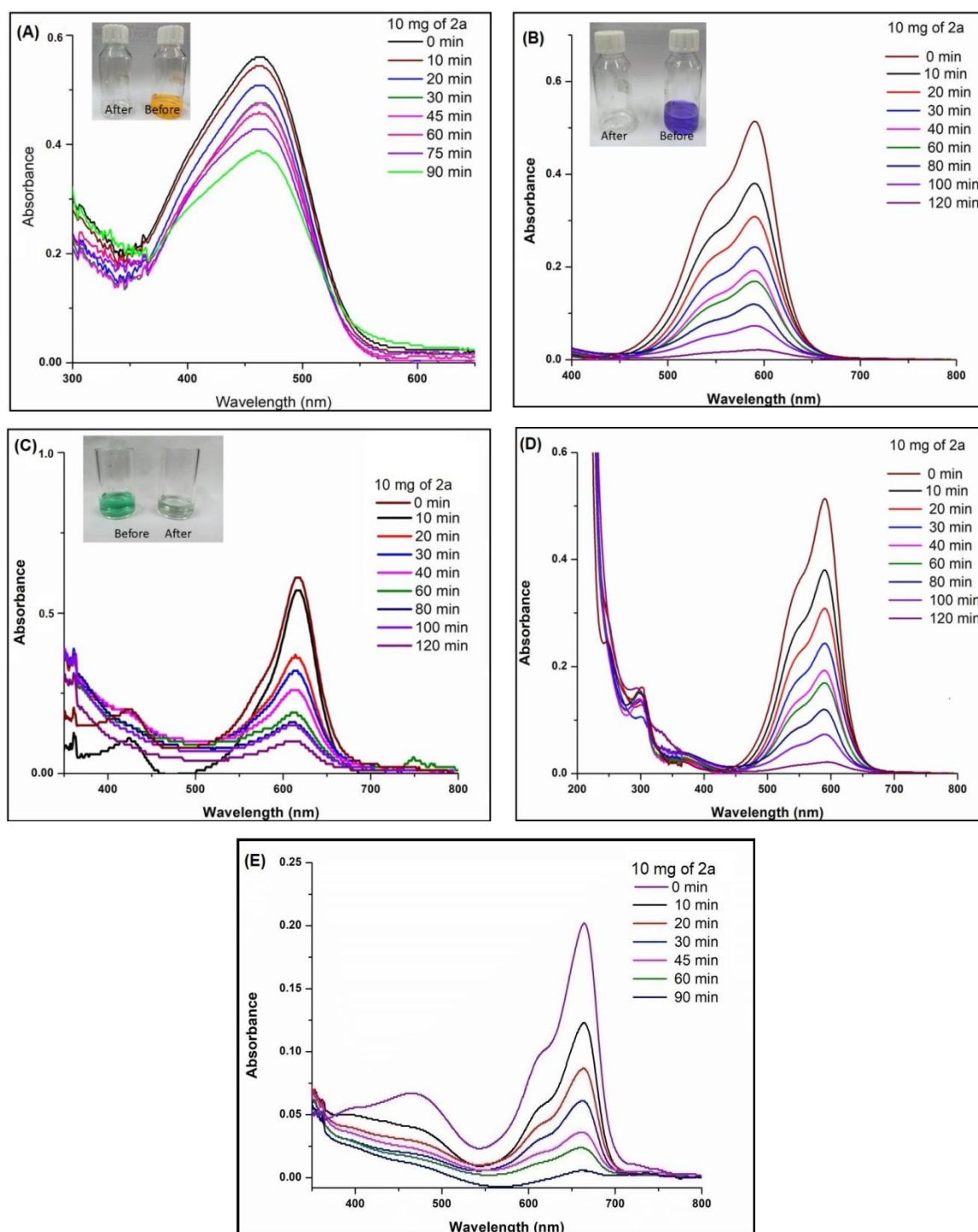


Fig. 6.16: Degradation of (A) MO, (B) CV, (C) MG, (D) CV+MG, (E) MO+MB, by 10 mg of **2a** in presence of sunlight, monitored by UV-Vis spectroscopy.

Effect of pH on the degradation of MB was also studied to check the efficiency of **2a** under different conditions. It was found that catalyst was highly active at neutral pH (**Fig. 6.17**). A comparative degradation efficiency of different nickel sulphide based photocatalysts towards dye degradation is presented in **Table 6.2**.

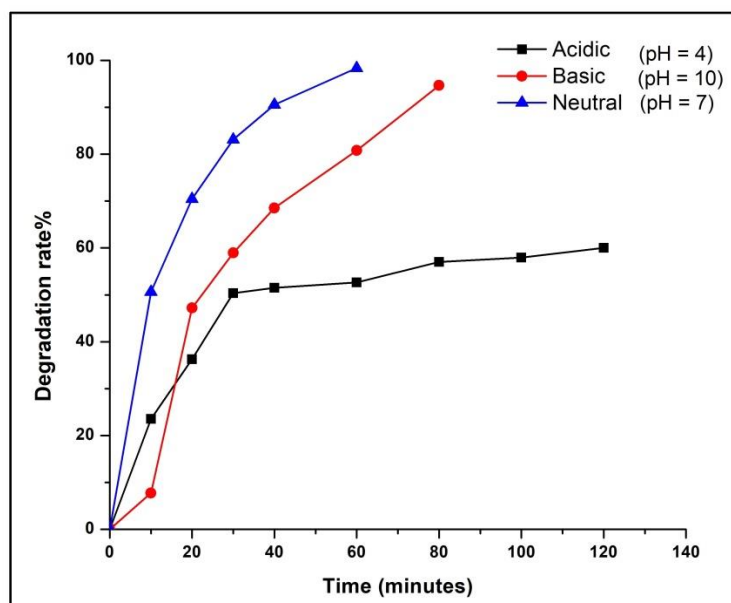


Fig. 6.17: Plot of degradation rates (%) of MB with respect to reaction time for 10 mg of **2a** under acidic, basic, and neutral conditions.

Table 6.2: Comparative degradation efficiency of different nickel sulphide based nanomaterials towards dye degradation.

Materials	Synthesis method	Light source	Dye	Photocatalytic degradation efficiency(%)	Irradiation time	Reference
NiS ₂ /CNS	One-step thermal condensation	300W Halogen lamp	RhB	91	180	[33]
Ni ₉ S ₈	Solvothermal	UV irradiation	MB	91	180	[34]
NiFeS ₂ and Ni ₂ FeS ₄			MB	95	180	
NiS	Hydrothermal	Solar lamp	MB	70	100	[35]
NiS/rGO			MB	87	100	

NiS ₂ /NP	Co-precipitation ultrasonic-assisted	UV irradiation	Indigo Carmine	99	180	[36]
NiS nanorods	Hydrothermal	Xenon lamp	MB	32	30	[37]
25% Co-NiS/S-g-C ₃ N ₄	Self-assembly technique		MB	98	32	
NiS	Hydrothermal	200W bulb	MB	89	70	[38]
NiS/CNT				96	50	
NiS	Grinding	sunlight	MB	98	60	This work

6.2.3.1 Active species for the degradation of dyes

To determine the active species involved in the degradation of MB, 1 mM of a scavenger was added to the dye solution. The scavengers used for this study were AgNO₃ for electrons e⁻, Na₂-EDTA for holes h⁺, i-PrOH for ·OH and benzoquinone (BQ) for ·O₂. **Fig. 6.18** shows that addition of scavengers reduced the rate of degradation of MB. Addition of AgNO₃ reduced the reaction rate by 86.26% indicating that electrons play a significant role in the degradation of MB. A decrease of 44.64% was noted in the degradation rate of MB on addition of the ·O₂ scavenging of benzoquinone. Further, on addition of h⁺ scavenging Na₂-EDTA and ·OH scavenging i-PrOH, decrease of 25.3% and 20.13% were observed in the degradation rate of MB. Thus, it can be concluded that electrons and ·O₂ species play a dominant role in the degradation mechanism. A plausible mechanism for the degradation of MB dye by **2a** is shown in **Fig. 6.19**. The conduction band (CB) electrons e⁻ might react with the dissolved oxygen to form reactive oxygen species (ROS) ·O₂. Similarly by the action of holes ·OH radicals are also generated. These radicals ·O₂/·OH together carry out the degradation of MB dye.

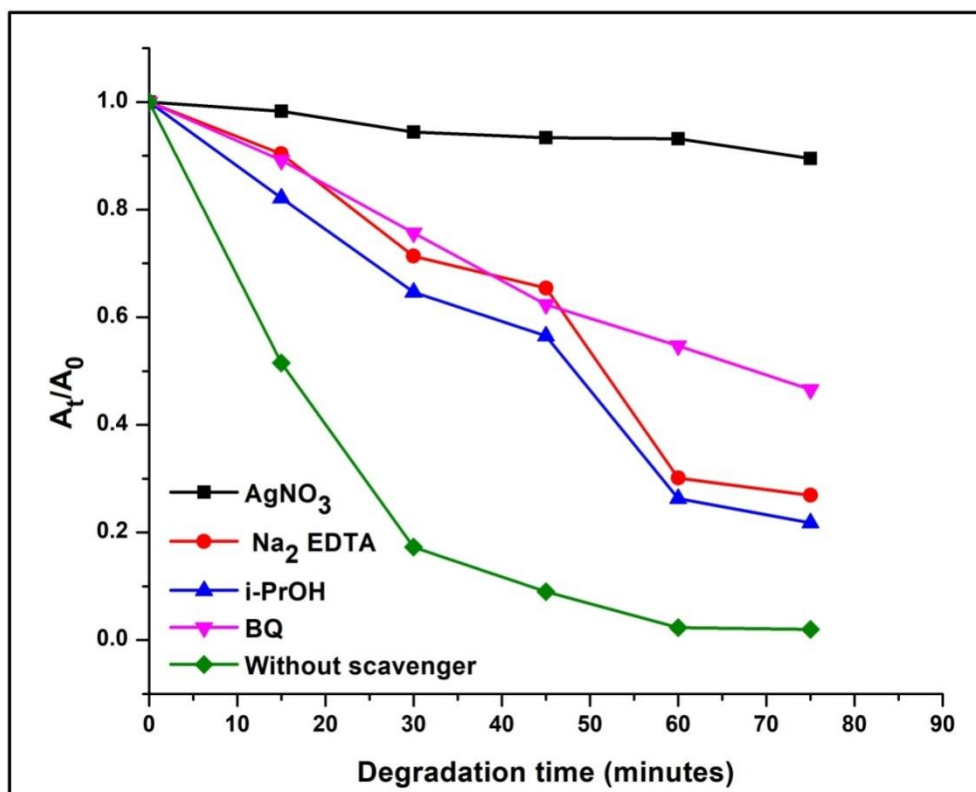


Fig. 6.18: Detection of active species in the degradation of MB by adding scavengers.

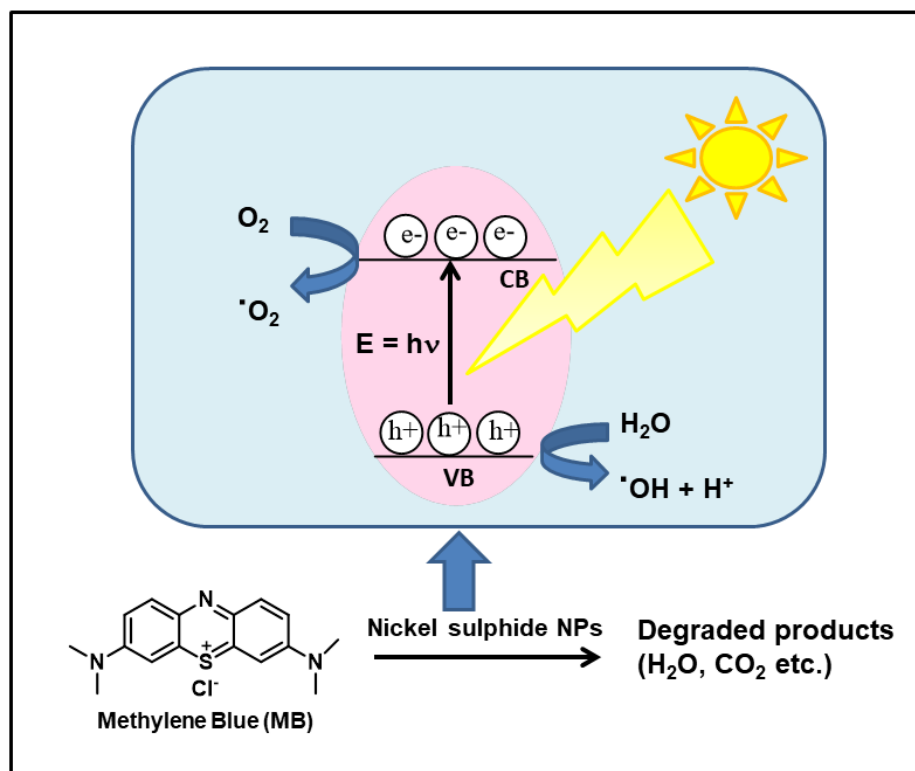
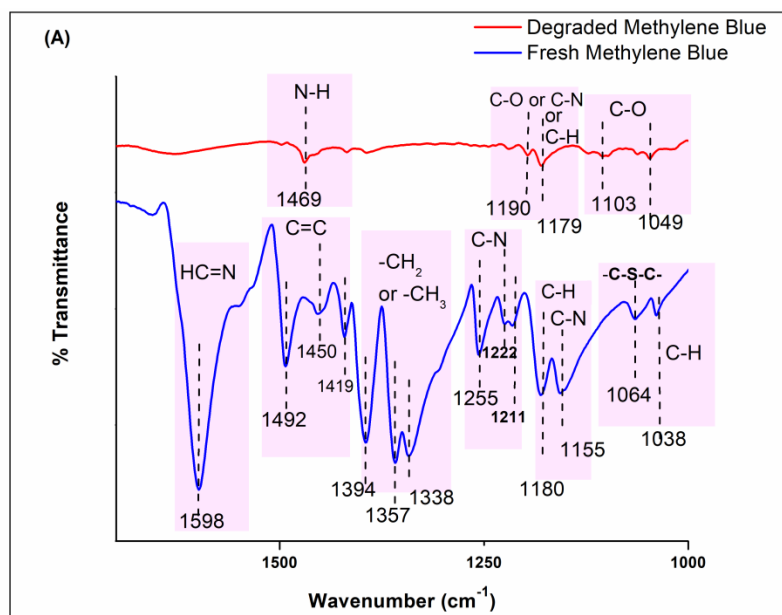


Fig. 6.19: Plausible mechanism for the degradation of MB by nickel sulphide NPs.

6.2.3.2 Evidence for degradation of dyes

The FT-IR spectra of the degraded MB alongside that of the fresh MB are given in **Fig. 6.20 (A&B)**. The characteristic peaks of MB in the finger-print region were observed at 1598 cm^{-1} (HC=N stretching), $1419\text{-}1490\text{ cm}^{-1}$ (C-N stretching), $1341\text{-}1395\text{ cm}^{-1}$ ($-\text{CH}_2$ or $-\text{CH}_3$ stretching), $1200\text{-}1250\text{ cm}^{-1}$ (C-N stretching), 1180 cm^{-1} (-CH in-plane bending vibrations), 1155 cm^{-1} (C-N stretching), 1064 cm^{-1} (-C-S-C- in plane vibrations) and 1038 cm^{-1} (-CH out of plane vibrations), in the FT-IR spectra of fresh MB [39]. Furthermore, -OH stretching vibrations at 3400 cm^{-1} and -CH symmetric and asymmetric vibrations were also observed at $2850\text{-}2924\text{ cm}^{-1}$ [39]. After photocatalytic degradation of MB dye, the FT-IR spectra indicates that the main chromophores are completely decomposed to H-OH (3419 cm^{-1}), C-H (2917 and 2852 cm^{-1}), C=O (1739 cm^{-1}), N-H (1469 cm^{-1}), C-H, C-N or C-O ($1170\text{-}1200\text{ cm}^{-1}$) and C-O ($1000\text{-}1100\text{ cm}^{-1}$), which evidently indicates that MB has been successfully degraded by **2a**. The conjugate structure of the N-S heterocyclic MB was broken down during the photocatalytic degradation process into smaller molecules like CO_2 , H_2O , amines, carboxylic acids and other mineralized products.



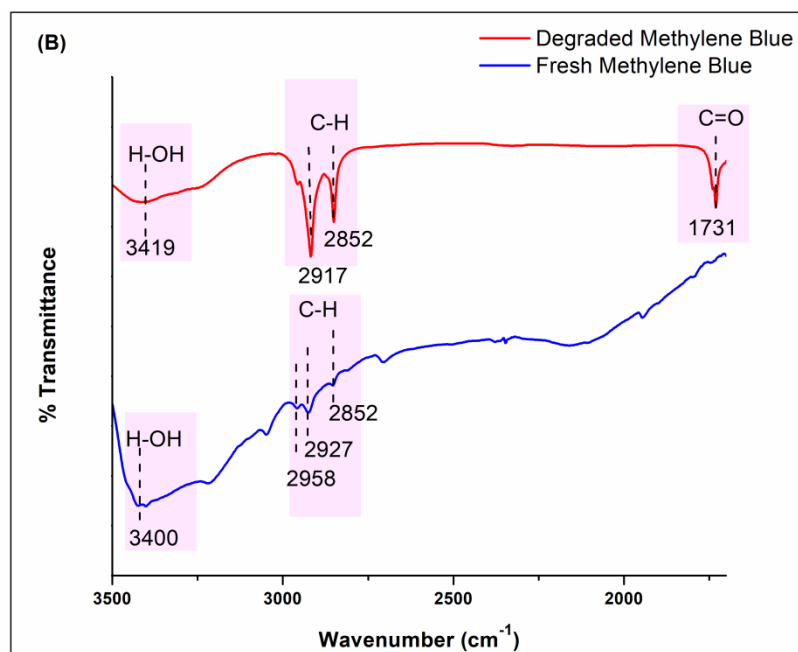


Fig. 6.20: FT-IR spectra of methylene blue (MB) in (A) 1000-1700 cm⁻¹ and (B) 1700-3500 cm⁻¹ region before and after degradation.

Fig. 6.21 displays the MB degradation (%) and TOC removal (%) at optimized conditions (10 mg of **2a**, pH 7). It was observed that MB dye was completely degraded by **2a** under these conditions, yielding 98.38% degradation efficiency and 79.20% TOC removal.

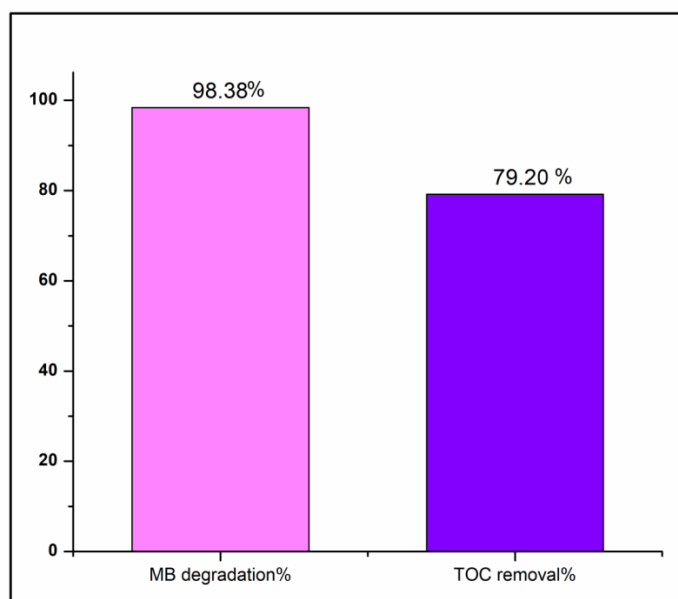


Fig. 6.21: MB degradation (%) and TOC removal% at optimized conditions.

6.2.3.3 Recyclability of the catalyst

The reusability of **2a** as a catalyst for the degradation of MB dye was studied for five consecutive runs (**Fig. 6.22**). At the end of 5th cycle the degradation rate for MB was 65.30%. Recovery of the catalyst **2a** was done by filtration of the degraded solution, followed by washing it with water and diethyl ether to remove inorganic and organic byproducts. The retention of the PXRD diffraction peaks of the reused catalyst **2a** can be seen in **Fig. 6.23**.

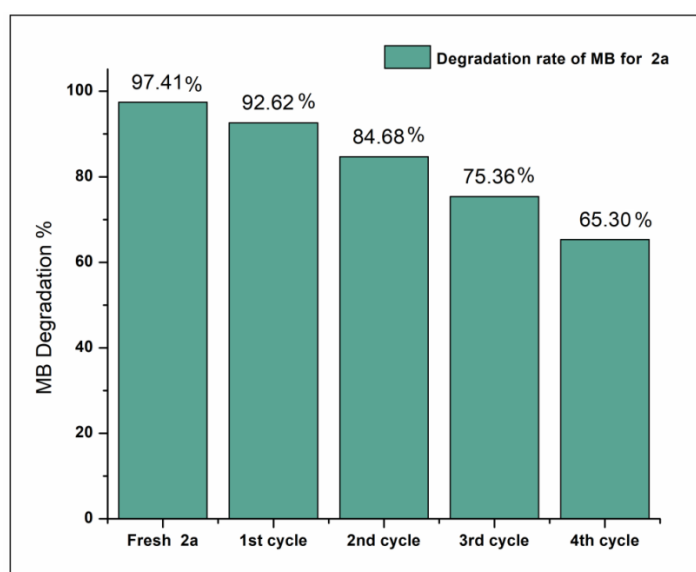


Fig. 6.22: Degradation rate% of MB dye by **2a** for five consecutive runs.

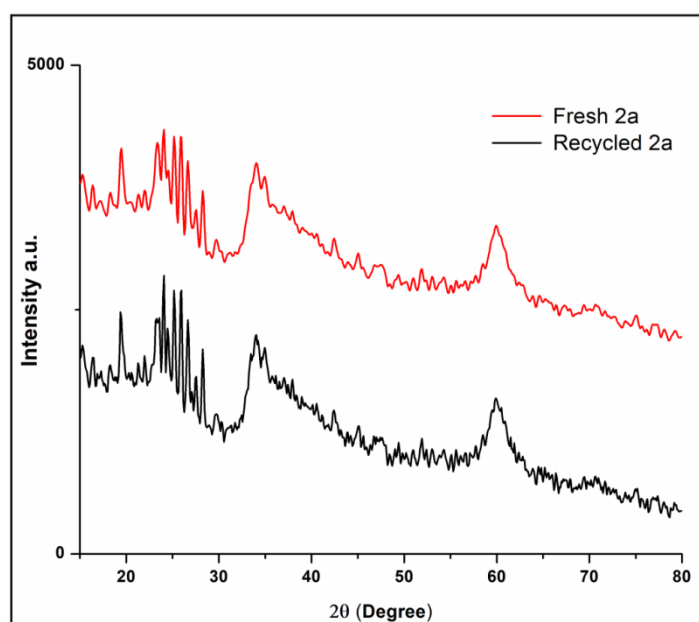


Fig. 6.23: PXRD pattern of **2a** (recycled) with the fresh **2a**.

6.3 Summary

This work was focussed on the applications of halometallate ionic liquids as precursor/template in the synthesis of nickel sulphide nanoparticles. The nickel sulphide nanoparticles were synthesized using a simple grinding method and were characterized using various analytical techniques. The EDX and XP spectra of the nanoparticles confirmed the presence of both nickel and sulphur. The PXRD pattern of the synthesised nanoparticles indicated the existence of both rhombohedral β -NiS phase and orthorhombic α -NiS phase. The TEM analysis revealed the formation nickel sulphide nanosheets with average particle size between 20-35 nm. The surface area values of the nanoparticles **2a** and **2b** were evaluated from their nitrogen adsorption-desorption isotherms and were found to be 22.27 m²/g and 13.68 m²/g respectively. The estimated band gap value of **2a** was found to be 2.39 eV and that of **2b** was found to be 2.80 eV. Based on these results, the nanoparticles **2a** and **2b** were used as photocatalysts in the degradation of organic dyes (MB, MO, CV, MG and their mixtures) under sunlight where **2a** exhibited slightly better catalytic activity compared to **2b**.

6.4 Experimental Section

6.4.1 Synthesis of the N-SO₃H functionalized imidazolium based chloronickellates

The N-SO₃H functionalized imidazolium ionic liquids [RSIM]_x[NiCl_y], (where R = C₂H₅& CH₃, x =2, y = 2, 3,4,5) were prepared following the standard procedure in a two-step method (**Scheme 6.1**) [21]. The first step involves dissolving 20 mmol of 2-ethylimidazole or 2-methylimidazole in 10 mL of dry DCM (CH₂Cl₂) in a two neck 100 mL round bottomed flask. It was then stirred for 15 min and chlorosulfonic acid (40 mmol) was added drop wise to this stirred solution over a period of 3 min at 0 °C to prepare the initial ionic liquid [RSIM][Cl]. The DCM solution was evaporated under reduced pressure to isolate the viscous chloride based [RSIM][Cl] IL. The second step was performed by mixing nickel chloride (NiCl₂ with the [RSIM][Cl] in the mole ratio of 1:2 (NiCl₂:[RSIM][Cl]). The reaction mixture was stirred at 60 °C in an oil bath for 2-3 hours and a light green chloronickelate ionic liquid [RSIM]_x[NiCl_y] with paste like consistency was formed. It was washed with dry CH₂Cl₂ (2 x 5 mL) and then dried in the vacuum oven at 80 °C for 2-3 hours to obtain analytically pure chloronickellate.

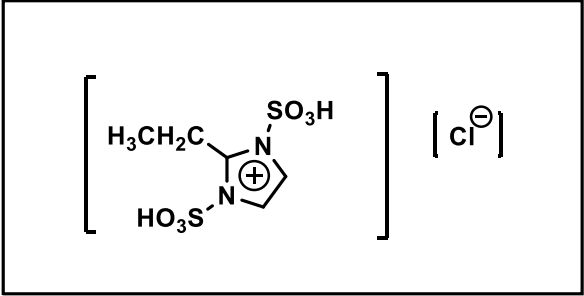
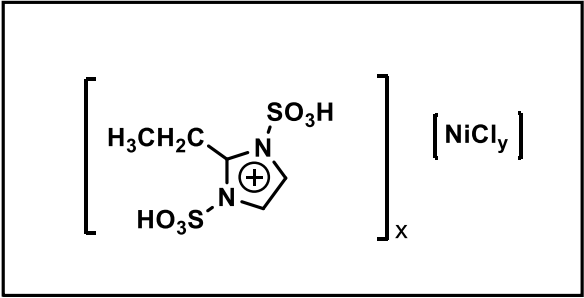
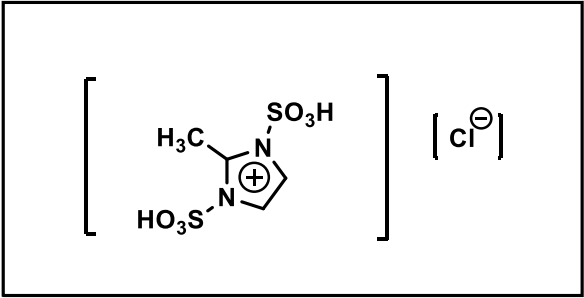
6.4.2. Synthesis of nickel sulphide nanoparticles using N-SO₃H functionalized imidazolium based chloronickellates as precursor and template

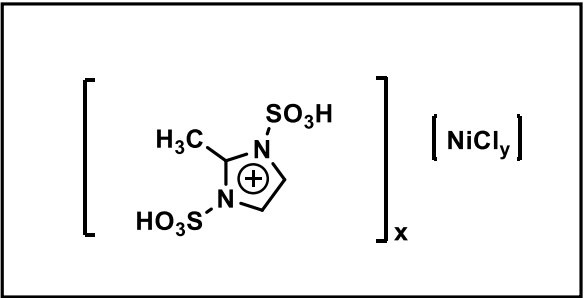
For the preparation of nickel sulphide nanoparticles, an equimolar amount of [RSIM]_x[NiCl_y] and sodium sulphide (Na₂S) were grounded in a mortar for 10 minutes [3] to form black colour Nickel sulphide (NiS) nanoparticles (NPs) (**2a** or **2b**) (Scheme 6.2). To remove any unreacted IL and NaCl formed during the reaction, the obtained nanoparticles were washed thrice with excess of double distilled water and then with ethanol. The obtained nickel sulphide nanoparticles were air dried for 24 hours and then they were dried in the vacuum oven at 80 °C for 3-4 hours.

6.4.3. General procedure for degradation of organic dyes using nickel sulphide nanoparticles

10 ppm aqueous solutions of the organic dyes (MB, MO, MG & CV) were prepared. 30 mL of a 10 ppm solution of dye was taken in a beaker and 10 mg of nickel sulphide nanoparticles (**2a**) were dispersed into it. The suspension was magnetically stirred under dark for 120 min to establish the adsorption-desorption equilibrium. Once the equilibrium is established, the reaction mixture was placed under direct sunlight for the photocatalytic degradation of the dye molecules. At given time intervals, 2 mL aliquots were taken from the reaction mixture and were centrifuged to remove the catalyst. The progress of the degradation was then monitored by recording the UV-Vis spectra of these experimental solutions collected at certain intervals with 1:1 dilution.

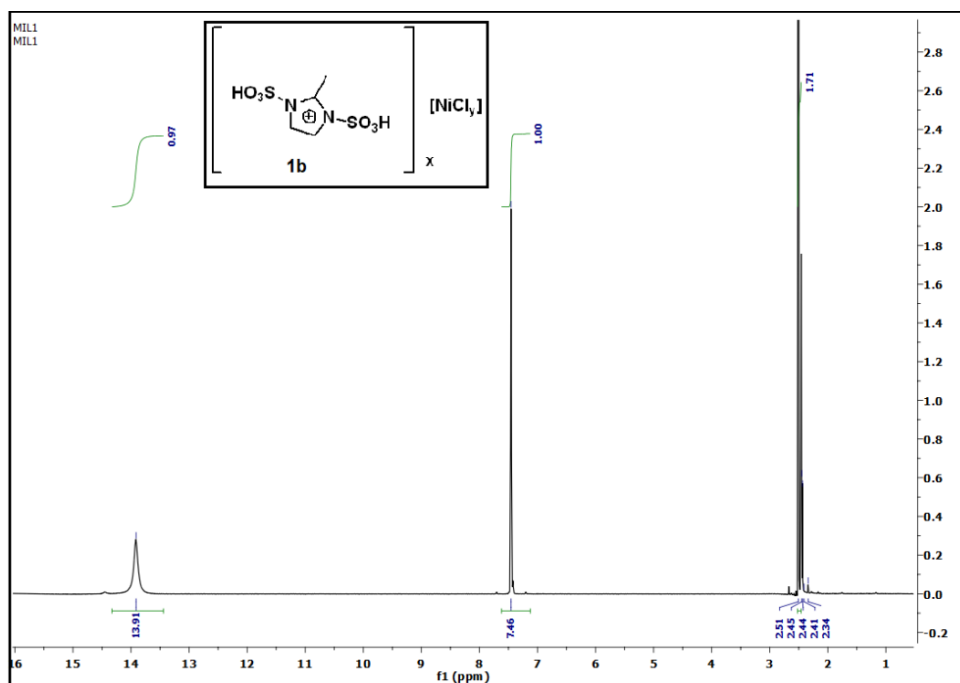
6.4.4 Spectral data of the ILs

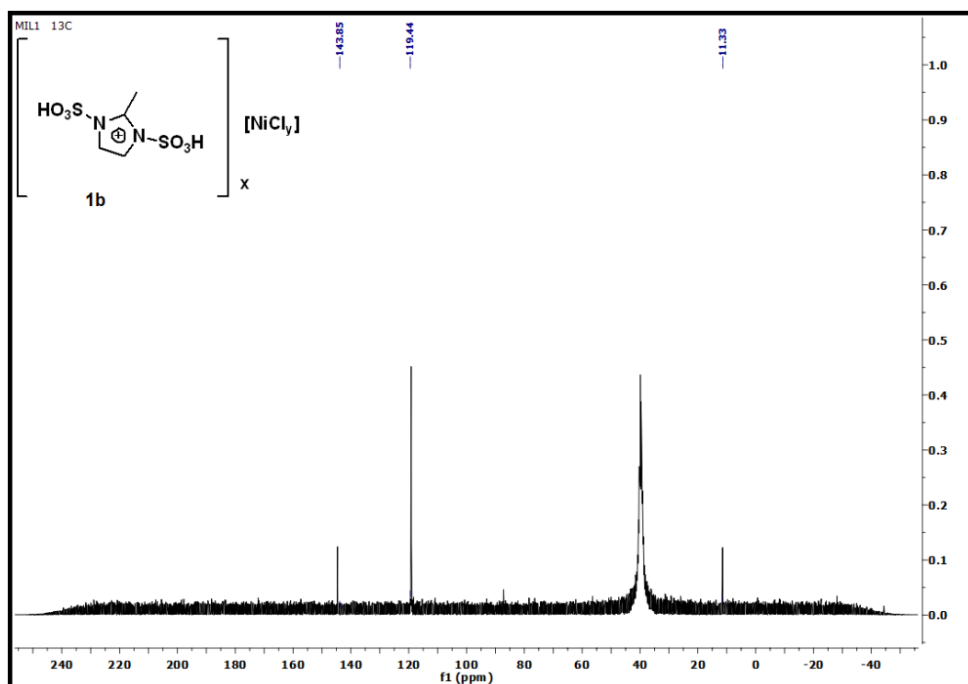
Sl.No.	Ionic liquid	Spectral data
1	 <p>2-ethyl-1,3- disulfoimidazolium chloride [EDSIM][Cl]</p>	Yellow viscous liquid; FT-IR (KBr) ν cm^{-1} : 3437, 2929, 2860, 1629, 1453, 1176, 1054, 872, 750, 581; ^1H NMR (DMSO- d_6 , 400 MHz): δ 13.94 (s, 1H) 13.0 (s, 1H), 7.47-7.42 (m, 2H), 2.88-2.84 (m, 2H), 1.24-1.17 (m, 3H); ^{13}C NMR (DMSO- d_6 , 100 MHz): δ 149.1, 119.1, 19.2 and 11.7.
2	 <p>2-ethyl-1,3- disulfoimidazolium chloronickellate (1a)</p>	Light green paste; FT-IR (KBr) ν cm^{-1} : 3424, 2929, 2855, 1622, 1543, 1462, 1171, 1063, 875, 753 and 579; ^1H NMR (DMSO- d_6 , 400 MHz): δ 13.95 (s, 1H) 12.96 (s, 1H), 7.47-7.42 (m, 2H), 2.90-2.79 (m, 2H), 1.26-1.17 (m, 3H); ^{13}C NMR (DMSO- d_6 , 100MHz): δ 149.1, 118.4, 19.6 and 11.3.ESI-HRMS m/z : 751.2576, 735.2849, 721.2721, 719.3081, 701.4686.
3	 <p>2-methyl-1,3-disulfoimidazolium chloride [MDSIM][Cl]</p>	Yellow viscous liquid; FT-IR (KBr) ν cm^{-1} : 3425, 3067, 2917, 1627, 1445, 1191, 1050, 873, 753 and 580; ^1H NMR (DMSO- d_6 , 400 MHz): δ 13.91 (s, 1H), 11.93 (s, 1H), 7.43 (s, 2H), 2.51 (s, 3H); ^{13}C NMR

		(DMSO-d ₆ , 100 MHz): δ 144.9, 119.1 and 11.3.
4	 <p>2-methyl-1,3-disulfoimidazolium chloronickellate (1b)</p>	<p>Light green paste; FT-IR (KBr) ν cm⁻¹: 3477, 2919, 2865, 1622, 1441, 1194, 1047, 887, 746 and 584; ¹H NMR (DMSO-d₆, 400 MHz) δ 13.91 (s, 2H) 7.46 (s, 2H), 2.51-2.34 (m, 3H), ¹³C NMR (DMSO-d₆, 100 MHz): δ 143.8, 119.4, and 11.3. ESI-HRMS m/z: 905.6121, 717.4169, 679.4618.</p>

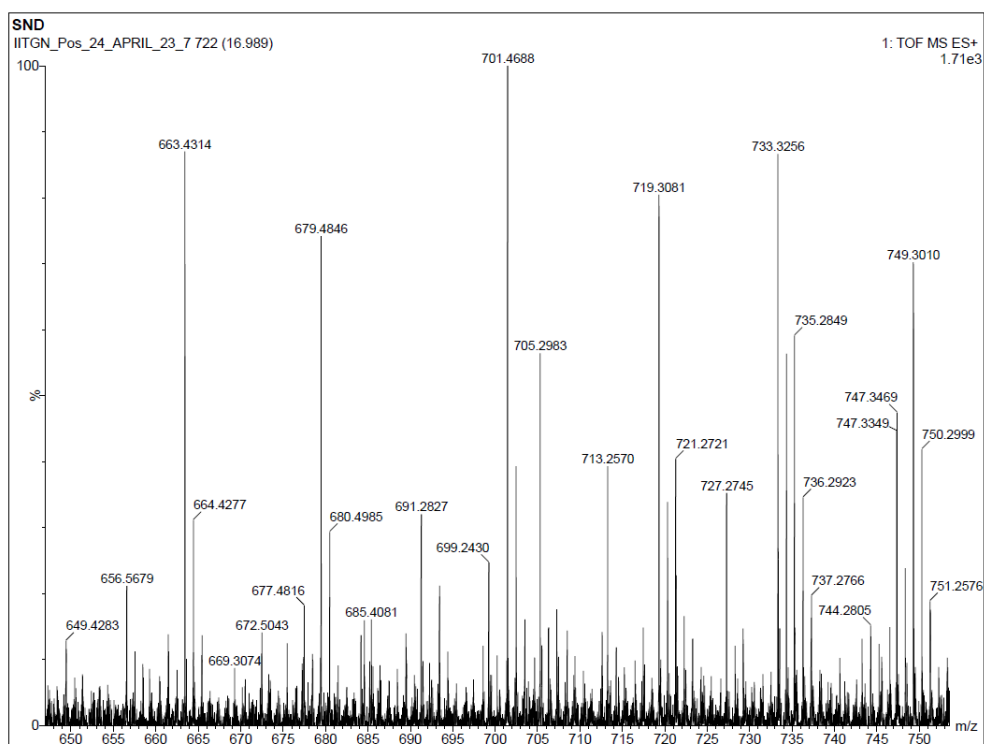
6.4.5 NMR spectra of imidazolium chloronickellate **1b**

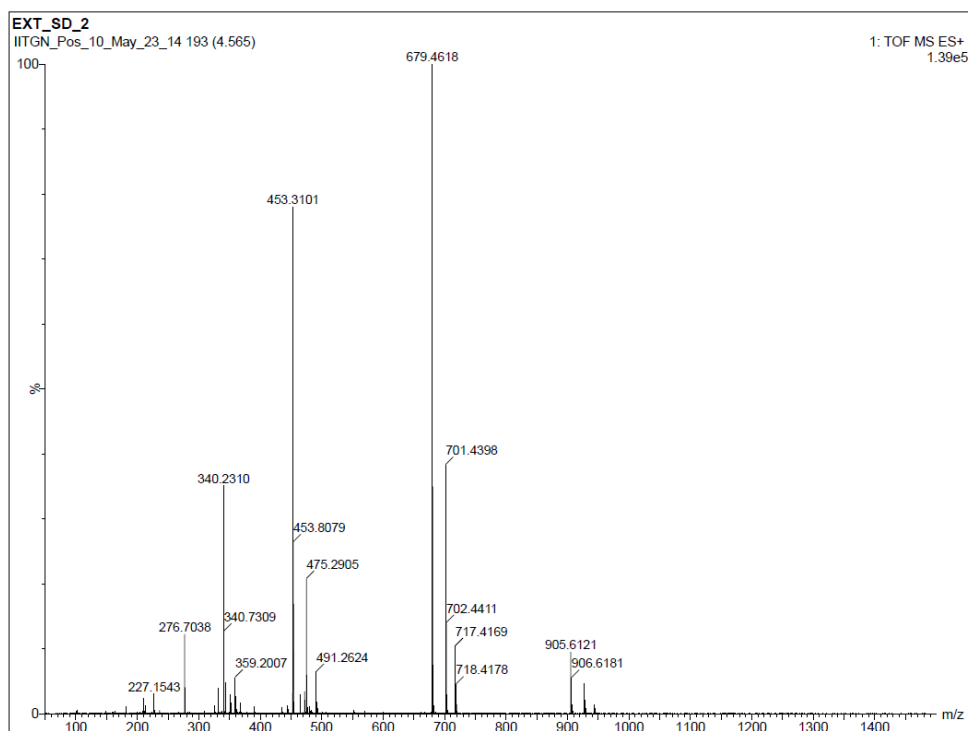
1. ¹H NMR spectra of **1b**



2. ^{13}C NMR spectra of **1b**

6.4.6 ESI-mass spectra of imidazolium chloronickellates

1. ESI-mass spectra of **1a**

2. ESI-mass spectra of **1b****Bibliography**

- [1] Verma, C., Ebenso, E. E., and Quraishi, M. A. Transition metal nanoparticles in ionic liquids: Synthesis and stabilization. *Journal of Molecular Liquids*, 276:826-849, 2019.
- [2] Narayanan, R. and El-Sayed, M. A. Catalysis with transition metal nanoparticles in colloidal solution: nanoparticle shape dependence and stability. *The Journal of Physical Chemistry B*, 109:12663-12676, 2005.
- [3] Arora, K., Shikha, P., and Kang, T.S. Facile and green one pot synthesis of zinc sulphide quantum dots employing zinc-based ionic liquids and their photocatalytic activity. *New Journal of Chemistry*, 41:7407-7416, 2017.
- [4] Liu, H., Song, C., Zhang, L., Zhang, J., Wang, H., and Wilkinson, D. P. A review of anode catalysis in the direct methanol fuel cell. *Journal of Power Sources*, 155:95-110, 2006.
- [5] Alayoglu, S., Nilekar, A. U., Mavrikakis, M., and Eichhorn, B. Ru–Pt core–shell nanoparticles for preferential oxidation of carbon monoxide in hydrogen. *Nature Materials*, 7:333-338, 2008.

- [6] Cheng, F., Liang, J., Tao, Z., and Chen, J. Functional materials for rechargeable batteries. *Advanced Materials*, 23:1695-1715, 2011.
- [7] Arora, K., Shikha, P., Kamal, M., and Kang, T. S. Modulation of morphological, optical and magnetic properties of Cr-doped La_{0.9}Ce_{0.1}FeO₃ nanoferrites synthesized by surface-active ionic liquid aided hydrothermal route. *Applied Physics A*, 127:1-9, 2021.
- [8] Arora, K., Singh, G., Karthikeyan, S., and Kang, T.S. One-pot sustainable preparation of sunlight active ZnS@ graphene nano-composites using a Zn containing surface active ionic liquid. *Nanoscale Advances*, 2:4770-4776, 2020.
- [9] Sekhar, M. C., Santhosh, K., Praveen Kumar, J., Mondal, N., Soumya, S., and Samanta, A. CdTe quantum dots in ionic liquid: stability and hole scavenging in the presence of a sulfide salt. *The Journal of Physical Chemistry C*, 118:18481-18487, 2014.
- [10] Wang, L., Xu, S. Z., Li, H. J., Chang, L. X., Zeng, M. H., Wang, L. N., and Huang, Y. N. Microbundles of zinc oxide nanorods: Assembly in ionic liquid [EMIM]⁺[BF₄]⁻, photoluminescence and photocatalytic properties. *Journal of Solid State Chemistry*, 184:720-724, 2011.
- [11] He, Z. and Alexandridis, P. Nanoparticles in ionic liquids: interactions and organization. *Physical Chemistry Chemical Physics*, 17:18238-18261, 2015.
- [12] Wegner, S. and Janiak, C. Metal nanoparticles in ionic liquids. *Topics in Current Chemistry*, 375:1-32, 2017.
- [13] Iida, M., Baba, C., Inoue, M., Yoshida, H., Taguchi, E., and Furusho, H. Ionic liquids of bis (alkylethylenediamine) silver (I) salts and the formation of silver (0) nanoparticles from the ionic liquid system. *Chemistry—A European Journal*, 14:5047-5056, 2008.
- [14] Xu, L., Xia, J., Wang, L., Qian, J., Li, H., Wang, K., Sun, K., and He, M. α -Fe₂O₃ Cubes with High Visible-Light-Activated Photoelectrochemical Activity towards Glucose: Hydrothermal Synthesis Assisted by a Hydrophobic Ionic Liquid. *Chemistry—A European Journal*, 20:2244-2253, 2014.
- [15] Liu, X., Ma, J., Peng, P., and Zheng, W. One-pot hydrothermal synthesis of ZnSe hollow nanospheres from an ionic liquid precursor. *Langmuir*, 26:9968-9973, 2010.

-
- [16] Estager, J., Holbrey, J. D., and Swadźba-Kwaśny, M. Halometallate ionic liquids—revisited. *Chemical Society Reviews*, 43:847-886, 2014.
- [17] Abbott, A. P., Frisch, G., and Ryder, K. S. Metal complexation in ionic liquids. *Annual Reports Section "A" (Inorganic Chemistry)*, 104:21-45, 2008.
- [18] Dupont, J., de Souza, R. F., and Suarez, P. A. Ionic liquid (molten salt) phase organometallic catalysis. *Chemical Reviews*, 102:3667-3692, 2002.
- [19] Zhang, J., Huang, C., Chen, B., Ren, P., and Lei, Z. Extraction of aromatic hydrocarbons from aromatic/aliphatic mixtures using chloroaluminate room-temperature ionic liquids as extractants. *Energy & Fuels*, 21:1724-1730, 2007.
- [20] Andreani, L. and Rocha, J.D. Use of ionic liquids in biodiesel production: a review. *Brazilian Journal of Chemical Engineering*, 29:1-13, 2012.
- [21] Saikia, S., Gogoi, P., Dutta, A. K., Sarma, P., and Borah, R. Design of multifaceted acidic 1, 3-disulfoimidazolium chlorometallate ionic systems as heterogeneous catalysts for the preparation of β -amino carbonyl compounds. *Journal of Molecular Catalysis A: Chemical*, 416:63-72, 2016.
- [22] Bodke, M. R., Purushotham, Y., and Dole, B. N. Comparative study on zinc oxide nanocrystals synthesized by two precipitation methods. *Cerâmica*, 64:91-96, 2018.
- [23] Sun, C., Ma, M., Yang, J., Zhang, Y., Chen, P., Huang, W., and Dong, X. Phase-controlled synthesis of α -NiS nanoparticles confined in carbon nanorods for high performance supercapacitors. *Scientific Reports*, 4:7054, 2014.
- [24] Nachimuthu, S., Kannan, K., Thangavel, S., and Gurushankar, K. Electrochemical and magnetic properties of 3D porous NiS/CuS nanocomposites. *Applied Surface Science Advances*, 7:100209, 2022.
- [25] Salavati-Niasari, M., Davar, F., and Emadi, H. Hierarchical nanostructured nickel sulfide architectures through simple hydrothermal method in the presence of thioglycolic acid. *Chalcogenide Lett*, 7:647-655, 2010.
- [26] Yoshikawa, M., Murakami, M., Matsuda, K., Matsunobe, T., Sugie, S., Okada, K., and Ishida, H. Characterization of Si nano-polycrystalline films at the nanometer level using resonant Raman scattering. *Journal of Applied Physics*, 98, 2005.
- [27] Molla, A., Sahu, M., and Hussain, S. Synthesis of tunable band gap semiconductor nickel sulphide nanoparticles: rapid and round the clock degradation of organic dyes. *Scientific Reports*, 6:26034, 2016.
-

- [28] Park, G. D., Cho, J. S., and Kang, Y. C. Sodium-ion storage properties of nickel sulfide hollow nanospheres/reduced graphene oxide composite powders prepared by a spray drying process and the nanoscale Kirkendall effect. *Nanoscale*, 7:16781-16788, 2015.
- [29] Luo, P., Zhang, H., Liu, L., Zhang, Y., Deng, J., Xu, C., Hu, N., and Wang, Y. Targeted synthesis of unique nickel sulfide (NiS, NiS₂) microarchitectures and the applications for the enhanced water splitting system. *ACS Applied Materials & Interfaces*, 9:2500-2508, 2017.
- [30] Karthikeyan, R., Thangaraju, D., Prakash, N., and Hayakawa, Y. Single-step synthesis and catalytic activity of structure-controlled nickel sulfide nanoparticles. *CrystEngComm*, 17:5431-5439, 2015.
- [31] Boruah, K., Bora, D. B., Saikia, S., and Borah, R. Study of photocatalytic properties of clay intercalated semiconductor composite material of guanidinium tetrachloroferrate for oxidative degradation of model dye in sunlight. *Journal of Materials Science: Materials in Electronics*, 33:2461-2478, 2022.
- [32] Jansi Rani, B., Dhivya, N., Ravi, G., Zance, S. S., Yuvakkumar, R., and Hong, S. I. Electrochemical performance of β -NiS@ Ni(OH)₂ nanocomposite for water splitting applications. *Acs Omega*, 4:10302-10310, 2019.
- [33] Jourshabani, M., Shariatinia, Z., Achari, G., Langford, C.H., and Badiei, A. Facile synthesis of NiS₂ nanoparticles ingrained in a sulfur-doped carbon nitride framework with enhanced visible light photocatalytic activity: two functional roles of thiourea. *Journal of Material Chemistry A*, 6:13448-13466, 2018.
- [34] Thirumaran, S., Gurumoorthy, G., Arulmozhi, R., and Ciattini, S. Synthesis of nickel sulfide and nickel-iron sulfide nanoparticles from nickel dithiocarbamate complexes and their photocatalytic activities. *Applied Organometallic Chemistry*, 34:e5761, 2020.
- [35] Arumugam, P., Sengodan, P., Duraisamy, N., Rajendran, R., and Vasudevan, V. An effective strategy to enhance the photocatalytic performance by forming NiS/rGO heterojunction nanocomposites. *Ionics*, 26:4201-4212, 2020.
- [36] Hafdi, H., Mouldar, J., Joudi, M., Hatimi, B., Nasrellah, H., Mhammedi, M.A.E., and Bakasse, M. Nickel sulfide impregnated on natural phosphate: characterization and applications in photocatalytic degradation of indigocarmine dye. *Optical and Quantum Electronics*, 53:1-13, 2021.

- [37] Abubshait, S.A., Iqbal, S., Abubshait, H.A., AlObaid, A.A., Al-Muhimeed, T.I., Abd-Rabboh, H.S., Bahadur, A., and Li, W. Effective heterointerface combination of 1D/2D Co-NiS/Sg-C₃N₄ heterojunction for boosting spatial charge separation with enhanced photocatalytic degradation of organic pollutants and disinfection of pathogens. *Colloids and Surfaces A: Physicochemical and Engineering Aspects*, 628:127390, 2021.
- [38] Haider, S., Shar, S.S., Shakir, I., and Agboola, P.O. Design of NiS/CNTs nanocomposites for visible light driven catalysis and antibacterial activity studies. *Ceramics International*, 47:34269-34277, 2021.
- [39] Alshehri, A. A., and Malik, M. A. Biogenic fabrication of ZnO nanoparticles using *Trigonella foenum-graecum* (Fenugreek) for proficient photocatalytic degradation of methylene blue under UV irradiation. *Journal of Materials Science: Materials in Electronics*, 30:16156-16173, 2019.